

JNCC Report No. 430: Appendix 4. MDAC Report



**British
Geological Survey**

NATURAL ENVIRONMENT RESEARCH COUNCIL

Petrography and stable isotope geochemistry of samples of methane-derived authigenic carbonates (MDAC) from the Mid Irish Sea

Marine Geosciences Programme
Commissioned Report CR/09/051

BRITISH GEOLOGICAL SURVEY

COMMISSIONED REPORT CR/09/051

Petrography and stable isotope geochemistry of samples of methane-derived authigenic carbonates (MDAC) from the Mid Irish Sea

A.E. Milodowski, A Lacinska and H Sloane

The National Grid and other Ordnance Survey data are used with the permission of the Controller of Her Majesty's Stationery Office.
Ordnance Survey licence number GD 272191/1999

Key words

MDAC, cold seep, methane oxidation, high-magnesian calcite, aragonite, dolomite, authigenic, Quaternary, Irish Sea, stable isotopes.

Bibliographical reference

MILODOWSKI, A E, LACINSKA, A AND SLOANE H. 2009. Petrography and stable isotope geochemistry of samples of methane-derived authigenic carbonates (MDAC) from the Mid Irish Sea. *British Geological Survey Commissioned Report, CR/09/051*. 63pp.

© NERC 2009

Keyworth, Nottingham British Geological Survey 2009

BRITISH GEOLOGICAL SURVEY

The full range of Survey publications is available from the BGS Sales Desks at Nottingham and Edinburgh; see contact details below or shop online at www.thebgs.co.uk

The London Information Office maintains a reference collection of BGS publications including maps for consultation.

The Survey publishes an annual catalogue of its maps and other publications; this catalogue is available from any of the BGS Sales Desks.

The British Geological Survey carries out the geological survey of Great Britain and Northern Ireland (the latter as an agency service for the government of Northern Ireland), and of the surrounding continental shelf, as well as its basic research projects. It also undertakes programmes of British technical aid in geology in developing countries as arranged by the Department for International Development and other agencies.

The British Geological Survey is a component body of the Natural Environment Research Council.

Keyworth, Nottingham NG12 5GG

☎ 0115-936 3241 Fax 0115-936 3488
e-mail: sales@bgs.ac.uk
www.bgs.ac.uk
Shop online at: www.thebgs.co.uk

Murchison House, West Mains Road, Edinburgh EH9 3LA

☎ 0131-667 1000 Fax 0131-668 2683
e-mail: scotsales@bgs.ac.uk

London Information Office at the Natural History Museum (Earth Galleries), Exhibition Road, South Kensington, London SW7 2DE

☎ 020-7589 4090 Fax 020-7584 8270
☎ 020-7942 5344/45 email: bgs london@bgs.ac.uk

Forde House, Park Five Business Centre, Harrier Way, Sowton, Exeter, Devon EX2 7HU

☎ 01392-445271 Fax 01392-445371

Geological Survey of Northern Ireland, 20 College Gardens, Belfast BT9 6BS

☎ 028-9066 6595 Fax 028-9066 2835

Maclean Building, Crowmarsh Gifford, Wallingford, Oxfordshire OX10 8BB

☎ 01491-838800 Fax 01491-692345

Parent Body

Natural Environment Research Council, Polaris House, North Star Avenue, Swindon, Wiltshire SN2 1EU

☎ 01793-411500 Fax 01793-411501
www.nerc.ac.uk

Foreword

This report is the published product of a study by the British Geological Survey (BGS) commissioned by Cefas

Acknowledgements

Dr David Long and Dr Alick Leslie (BGS) are acknowledged for providing background information on the MDAC samples and helpful discussions on the interpretation of the data.

Contents

Appendix 4. MDAC Report	143
Foreword	146
Acknowledgements	146
Contents	147
Figures	147
Plates	148
Tables	150
Summary	151
Introduction	153
2.1 General	153
Samples	153
Geological background	155
Analytical methods	157
3.1 Petrographical analysis	157
3.1.1 Polished section and polished block preparation	157
3.1.2 Optical microscopy	157
3.1.3 Cathodoluminescence microscopy	157
3.1.4 Scanning electron microscopy and electron probe microanalysis	157
3.2 X-ray diffraction analysis	158
3.3 Stable isotope analysis	158
Mineralogy and petrography	160
4.1. Sample ST12 Sledge	160
Sample ST21 G09	170
Sample ST22 G05	177
4.4 Sample ST27 G22	182
4.5 Sample ST35 G17	191
4.6 Sample ST36 RD04	192
Stable isotope characteristics	196
5.1 General	196
5.2 Carbon isotope composition	196
5.3 Oxygen isotope composition	197
Summary and conclusions	201
References	203

Figures

Figure 58. Location map of the area of study in the Mid Irish Sea from Cefas cruise CEND 11/08 (blue box), with generalised bathymetry and multibeam data from SEAS 6 study (taken from Whormersley <i>et al.</i> , 2008).....	154
Figure 59. Summary diagram of survey lines and sampling points at Submarine Structures in the Mid Irish Sea area of study (taken from Whormersley <i>et al.</i> , 2008).	155
Figure 60. CaCO ₃ -MgCO ₃ -SrCO ₃ molar ratio plot illustrating the composition of the aragonite cement in MDAC sample “ST12 Sledge”, relative to end-member carbonate minerals	164
Figure 61. CaCO ₃ -MgCO ₃ -FeCO ₃ molar ratio plot illustrating the composition of the carbonate cements in MDAC sample “ST21 G09”, relative to end-member carbonate minerals	174

Figure 62. CaCO ₃ -MgCO ₃ -FeCO ₃ molar ratio plot illustrating the composition of the carbonate cements in MDAC sample “ST22 G05”, relative to end-member carbonate minerals.....	180
Figure 63. XRD trace for bulk MDAC sample ST27 G22 and comparison with reference patterns (“stick patterns”) for potential carbonate minerals	187
Figure 64. CaCO ₃ -MgCO ₃ -SrCO ₃ molar ratio plot illustrating the composition of the carbonate cements in MDAC sample “ST27 G22”, relative to end-member carbonate minerals.....	188
Figure 65. XRD trace for bulk MDAC sample ST36 RD04 and comparison with reference patterns (“stick patterns”) for potential carbonate minerals	195
Figure 66. Cross-plot of δ13C and δ18O illustrating the variation in stable isotopic composition for the MDAC samples	196

Plates

Plate 1. Transmitted light photomicrograph (crossed polars) at the interface between a densely-carbonate cemented (birefringent area) and porous weakly cemented (dark area) MDAC sandstone. The rock has a very open quartz grain fabric, and displays three generations of carbonate cement: (1) early isopachous grain-fringing aragonite, enclosed beneath; (2) dense micritic or microsparry aragonite, and; (3) later acicular (needles) aragonite lining open pores. Sample ST12 Sledge.	161
Plate 2. Transmitted light photomicrograph (crossed polars) showing abundant disseminated brownish fine sand- to silt-grade botryoidal or pelloidal grains composed of fine grained birefringent aragonite and fine-to medium sand-grade quartz (white), encrusted with acicular (needles) aragonite lining open porosity (black). Sample ST12 Sledge.....	161
Plate 3. BSEM image showing a fragment of bivalve shell (1), coated with very thin isopachous aragonite fringe cement (2) from which later acicular aragonite cement (3) has nucleated. Sample ST12 Sledge.....	162
Plate 4. BSEM image showing the growth of needles of aragonite into open intergranular pores. The aragonite has nucleated on the surface of clay-rich “pellets” or “clots” or grain-coating clay pellicles (fine dark grey material). Sample ST12 Sledge.	162
Plate 5. BSEM image showing the tightly-interlocking microcrystalline fabric of the “clots” or “pellets” of aragonite that form the locally densely-cemented domains of MDAC sandstone. In more open pore space, the aragonite develops equant euhedral crystal form. Sample ST12 Sledge.	163
Plate 6. BSEM image displaying the tightly-interlocking micritic microcrystalline fabric of the “clots” or “pellets” of aragonite that form the locally densely-cemented domains of MDAC sandstone. Aragonite nucleated on the surfaces of these “pellets” has grown as needles into the open pores. Sample ST12 Sledge.	163
Plate 7. Transmitted light photomicrograph (plane-polarised light) showing moderately-sorted, very fine to medium sandstone, composed of dominantly of angular detrital quartz grains (clear) and subordinate detrital K-feldspar and plagioclase (cloudy grains). [The rock is cemented by fine-grained, patchy micritic dolomite that appears dark brown to semi-opaque due to staining with disseminated fine iron oxide. Sample ST21 G09.....	170
Plate 8. Transmitted light photomicrograph (plane-polarised light) showing sub-angular and sub-rounded detrital quartz (clear) and partially altered feldspar (cloudy) sand grains. A well-rounded grain of fresh glauconite (green) is also seen. Fine-grained, brown to semi-opaque dolomicrite forms the intergranular matrix and also forms a “pelloidal” fabric that appears to have a similar grain size to the quartz sand grains. Sample ST21 G09.....	171

Plate 9. Transmitted light photomicrograph (crossed-polars) showing angular detrital quartz and a well-preserved calcareous multi-chambered foraminiferal test. The detrital grains are bonded by highly birefringence isopachous fine-grained dolomite cement forming a grain-coating fringe or meniscus. Fine-grained, semi-opaque dolomicrite fills the foraminiferal chambers and occurs as irregular patches and “silt-grade pellets in the matrix. Sample ST21 G09.....	171
Plate 10. BSEM image showing clusters of microspheroidal aggregates of dolomite forming locally porous intergranular cement. Denser areas of dolomite cement are partially cemented or replaced by later siderite (bright) filling micropores in the dolomite cement. Sample ST21 G09.....	172
Plate 11. BSEM image showing rounded limestone grain (centre) with early isopachous dolomite fringe cement. The interstitial matrix is partially cemented by spheroidal clusters of fine microporous dolomite in which siderite (bright) partially fills the microporosity. Sample ST21 G09.....	173
Plate 12. BSEM image showing detail of the microfabric of the microporous dolomite cement. The dolomite consists of “framboidal” aggregates of rhombic dolomite microcrystals, often nucleated around a “hollow core”. Sample ST21 G09.	173
Plate 13. Transmitted light photomicrograph (plane polarised light) of dolomite-cemented fine to medium sandstone, showing angular to sub-angular detrital quartz sand cemented by patchy brown to opaque microdolosparite cement. Sample ST22 G05.....	177
Plate 14. Transmitted light photomicrograph (crossed-polars) showing the development of an early grain-fringing isopachous microdolosparite cement (highly birefringent). Dolomicrite or microsparry dolomite also forms very fine to fine sand-grade “clots” or “pellets”. Sample ST22 G09.....	178
Plate 15. BSEM image showing isopachous microdolospar cement fringes around detrital sand grains, and “clots”, or spheroidal-framboidal aggregates of dolomite microcrystals within the intergranular areas. Sample ST22 G05.....	178
Plate 16. BSEM image showing detail of the microfabric of the microporous dolomite cement. The dolomite consists of “microbotryoidal” or “framboidal” aggregates of rhombic dolomite microcrystals, often nucleated around a “hollow core”. Sample ST22 G05.	179
Plate 17. BSEM image showing clusters of very fine cellular structures partially mineralised by dolomite, and associated with framboidal or spherical aggregates of dolomite microcrystals. Sample ST22 G05.	179
Plate 18. Transmitted light photomicrograph (plane-polarised light) showing porous sand fabric with intergranular pores (blue) lined or partially-filled by fibrous or acicular aragonite crystals, resting on brownish micritic high-magnesium calcite grain-coating fringes. Sample ST27 G22.....	182
Plate 19. BSEM image showing early spherical clusters or “clots” of microcrystalline (microsparry high-magnesium calcite (mid grey) encrusted by later needles of aragonite. Sample ST27 G22.....	183
Plate 20. BSEM image showing detail of microcrystalline aggregates of high-magnesium calcite (mid grey) encrusted by later needles of aragonite. Sample ST27 G22.....	183
Plate 21. BSEM image of more densely-cemented region of the MDAC sandstone, displaying a matrix cemented by micritic high-magnesium calcite. Fragments of detrital limestone and calcareous microfossils (light grey) can also be seen. ST27 G22.....	184
Plate 22. Transmitted light photomicrograph (crossed-polars) of same area as Plate 18, showing highly birefringent acicular aragonite lining intergranular porosity. Sample ST27 G22.....	185

Plate 23. SEM image showing acicular aragonite crystals (needles) nucleated around microporous spherical aggregates of microsparry or micritic high-magnesium calcite. Sample ST27 G22.....	185
Plate 24. SEM image showing detail of the crystal morphology of the aragonite needles. The crystals display bladed orthorhombic prismatic crystal form. Sample ST27 G22.	186
Plate 25. BSEM image showing altered detrital carbonate grain that has dissolved after initially being overgrown by acicular aragonite. ST27 G22.....	186
Plate 26. Transmitted light photomicrograph (plane-polarised light) showing early microcrystalline fringe of high-magnesium calcite cement around detrital quartz grains, enclosed within a fine dense micritic high-magnesium calcite matrix. Framboidal brown to opaque iron oxide or iron oxyhydroxide (after oxidised pyrite) in concentrated on the surface of the earlier calcite fringe cement, and is also less abundantly, disseminated through the later micritic calcite matrix. Sample ST35 G17.....	191
Plate 27. BSEM image showing grain-coating fringes of microcrystalline high-magnesium calcite, and areas of intergranular porosity filled by denser microcrystalline high-magnesium calcite cement. Bright grains of iron oxyhydroxide can be seen close to the grain margins. Sample ST35 G17.....	192
Plate 28. Transmitted light photomicrograph (plane-polarised light) showing angular and subangular grains of detrital quartz (clear), feldspar (cloudy), glauconite (green) and shell fragments, cemented by a brownish micritic matrix of high-magnesium calcite. Sample ST36 RD04.....	193
Plate 29. Transmitted light photomicrograph (crossed polars) showing brownish birefringence of iron-stained micritic high-magnesium calcite forming intergranular matrix cement. Traces of early isopachous grain-fringing high-magnesium cement can be seen around some detrital grains. The micritic calcite cement displays a pelloidal fabric. Sample ST36 RD04.....	193
Plate 30. BSEM image showing angular detrital quartz sand with sand-grade pellets of silt and clay cemented by micritic high-magnesium calcite. Sample ST36 RD04.....	194
Plate 31. SEM image showing fine equant to rhombohedral crystallites of high-magnesium calcite forming an early grain coating fringe cement. Sample ST36 RD04.....	194

Tables

Table 13. List of MDAC samples submitted for petrological analysis.....	153
Table 14. Electron microprobe of carbonate cements and other carbonate components in sample ST12 SLEDGE	166
Table 15. Electron microprobe of carbonate cements and other carbonate components in sample ST21 G09.....	175
Table 16. Electron microprobe of carbonate cements and other carbonate components in sample ST22 G05.....	181
Table 17. Electron microprobe of carbonate cements and other carbonate components in sample ST27 G22.....	189
Table 18. Stable isotope analyses ($\delta^{13}\text{C}$ and $\delta^{18}\text{O}$) for bulk and microsampled carbonate components from the MDAC samples.....	199

Summary

This report describes the findings of a programme of work undertaken by the British Geological Survey (BGS) on behalf of Cefas to characterise six samples of carbonate-cemented sandy sediment, recovered from the seabed of the Mid Irish Sea during a survey of the Mid Irish Sea area (Cefas Cruise CEND 11/08). The study forms part of an assessment of the geomorphology, and the distribution and range of seabed habitats, within this area of interest. The survey is focussed on identifying and delineating habitats listed under Annex I of the 1992 EC Habitats Directive; in particular, the Annex I habitat *Submarine structures made by leaking gases* (Whormersley *et al.*, 2008).

The carbonate-cemented sediments can be categorised into 3 end-member types:

1. Aragonite-dominated cements with strontium-rich aragonite containing up to 2 mole% SrCO₃ in solid-solution
2. High-magnesium calcite-dominated cements
3. Dolomite-dominated cements.

The carbonates display a number of fabrics including: early isopachous grain-coating fringes on detrital grains; precipitation of “clots”, or framboidal microbotryoidal aggregates of micritic or microcrystalline carbonate that may coalesce to form a locally dense micritic matrix; and late-stage precipitation of acicular aragonite lining open pores and cavities in the cemented sandstone. Minor late-stage magnesium siderite was also found filling porosity in the dolomite cement and as overgrowths on dolomite crystals in sample ST21 G09. However, siderite was not found in any other samples.

Sample ST27 G22 can be regarded as a “hybrid” of Type 1 Type 2 carbonates. It consists of sandy sediment with high-magnesium calcite cements similar to those found in type 2. However, it displays the development of later-stage acicular aragonite cement lining open intergranular pores, similar to the late-stage aragonite found in Type 1 carbonates.

Sample ST36 RD04 has a distinctly different type of carbonate fabric. It contains abundant sand-grade pelloidal grains consisting of intimately admixed micritic high-magnesium calcite and abundant siliciclastic silt and clay. It is interpreted to represent carbonate-rich sediment that has biologically-reworked and incorporated into faecal pellets. Apart from minor development of fine grain-coating high-magnesium calcite, petrographical evidence suggests that most of the carbonate cement in this sample has not precipitated in situ.

Stable isotope analyses of the carbonate cements shows that they are strong depleted in ¹³C, ($\delta^{13}\text{C}_{\text{PDB}}$ values are range from -31 to -51‰), which is consistent with a diagenetic origin in which carbonate precipitation is related to methane oxidation. This is very characteristic of MDAC reported from elsewhere (Jensen *et al.*, 1992; Sakai *et al.*, 1992; Bohrmann *et al.*, 1998; Peckmann *et al.*, 2001; Muralidhar *et al.*, 2006; Forsberg *et al.*, 2007), and supports the conclusion that these Mid Irish Sea seabed carbonates also have an MDAC origin.

The $\delta^{18}\text{O}$ signature of the carbonate cements does not correspond to the composition of carbonates expected to precipitate under present-day seabed conditions. The aragonite and high-magnesium calcites –dominated MDAC samples are isotopically slightly heavier than in cements expected to have formed in equilibrium with present-day conditions. This may indicate that they formed under slightly cooler conditions than at present. The dolomite

cements show a relatively wide range in $\delta^{18}\text{O}$ values varying from values close to that predicted to form in equilibrium with seawater under present-day temperatures to dolomite which is slightly lighter than expected. This may indicate formation under slightly warmer conditions than at present. Alternatively, the dolomite may have formed metastably and not in equilibrium with seawater, which possibly supported by the observation that the dolomite has significant excess calcium (possibly indicating metastable formation of dolomite via a protodolomite precursor).

Both $\delta^{18}\text{O}$ and $\delta^{13}\text{C}$ values for the carbonate sample ST36 RD04 are slightly heavier than for the other MDAC samples. This may indicate mixture with a component of carbonate precipitated with bicarbonate derived from more open marine water, which may be consistent with evidence that much of the carbonate in this sample has been reworked.

Introduction

2.1 General

The British Geological Survey (BGS) in partnership with the Centre for Environment, Fisheries and Aquaculture Science (Cefas) and the University of Ulster undertook a survey of the Mid Irish Sea area (Cruise CEND 11/08) to assess the geomorphology, and the distribution and range of seabed habitats, within this area of interest. Interest was focussed on identifying and delineating habitats listed under Annex I of the 1992 EC Habitats Directive; in particular, the Annex I habitat *Submarine structures made by leaking gases* (Whormersley *et al.*, 2008). These features are considered to be of important ecological significance and there is a requirement to adequately characterise these features in order to develop appropriate conservation management plans for such habits in UK offshore waters. The structures consist of carbonate-cemented sediments that are believed to have a Methane-Derived Authigenic Carbonate (MDAC) origin. The location of the study area is shown in Figure 57.

Samples

As part of this survey a small number of potential MDAC samples were acquired in order to describe the biological communities which characterise these habitats, and for petrological analysis in order to characterise the nature and origin of the carbonate cementation. The location of the samples is shown in Figure 58. They were recovered from water depths of between 50 60 m below mean seal level (MSL) using a variety of sampling techniques including: grab sampling (designated “G” samples); rock dredge sampling (designated “RD” samples), and; material recovered from the seabed video camera sledge (designated “Sledge” samples). A subset of six of these samples was submitted to the BGS for petrological and stable isotope analysis (Table 13). This report describes the mineralogical, petrographical and stable (oxygen and carbon) isotope characteristics of these samples.

Table 1. List of MDAC samples submitted for petrological analysis

SURVEY STATION	SAMPLE NUMBER	DESCRIPTION
12	SLEDGE	Burrowed and encrusted crusts.
21	G09	Finely burrowed crust.
22	G05	Unburrowed crust
27	G22	Thin amalgamated, burrowed crusts
35	G17	Large, burrowed crust
36	RD04	Sandy, weakly cemented crust

Notes:

G – grab sample

RD – rock dredge sample

SLEDGE - collected at end of scan line MIS-C01 when sledge snagged on crust debris

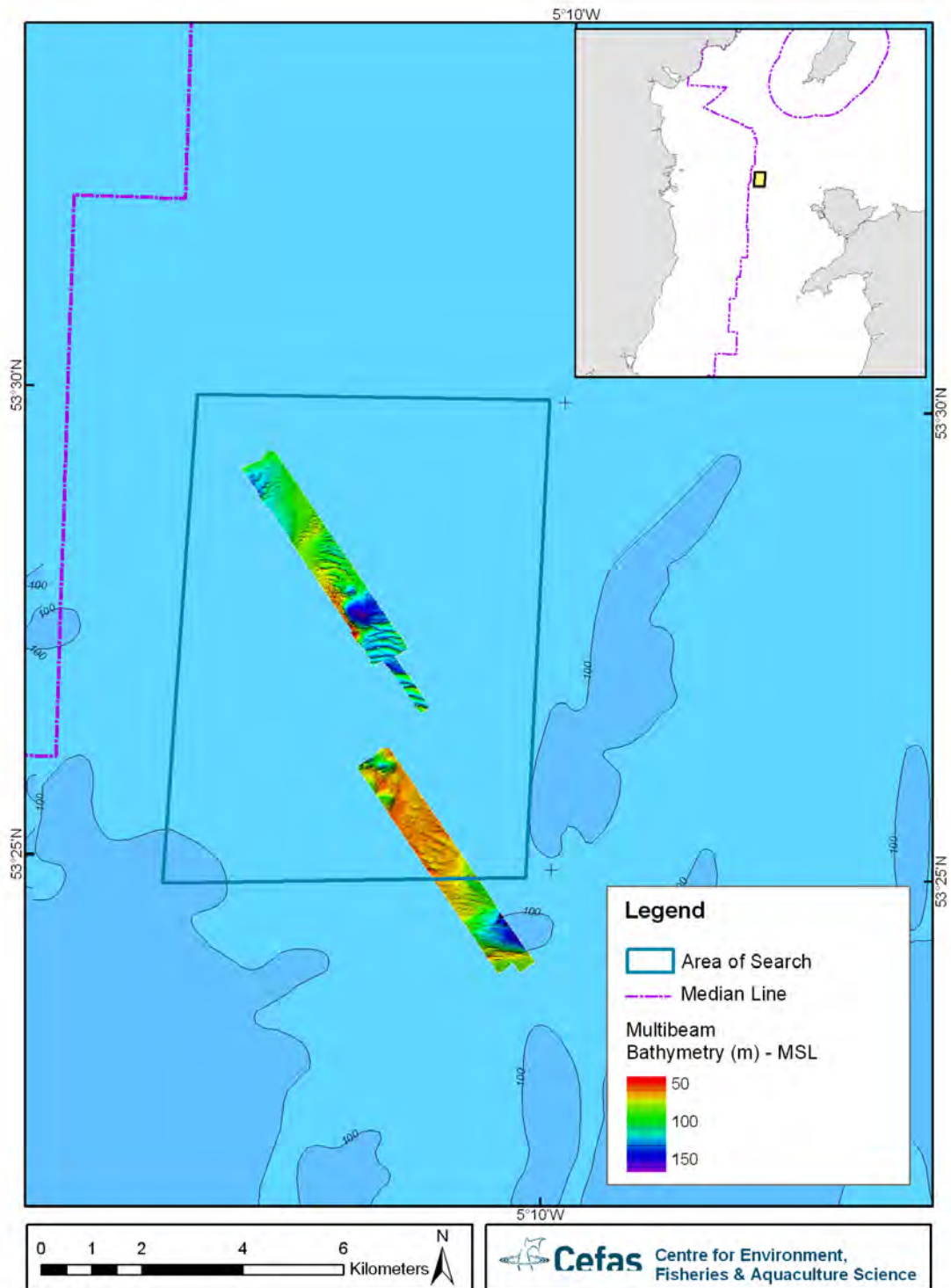


Figure 1. Location map of the area of study in the Mid Irish Sea from Cefas cruise CEND 11/08 (blue box), with generalised bathymetry and multibeam data from SEAS 6 study (taken from Whormersley *et al.*, 2008).

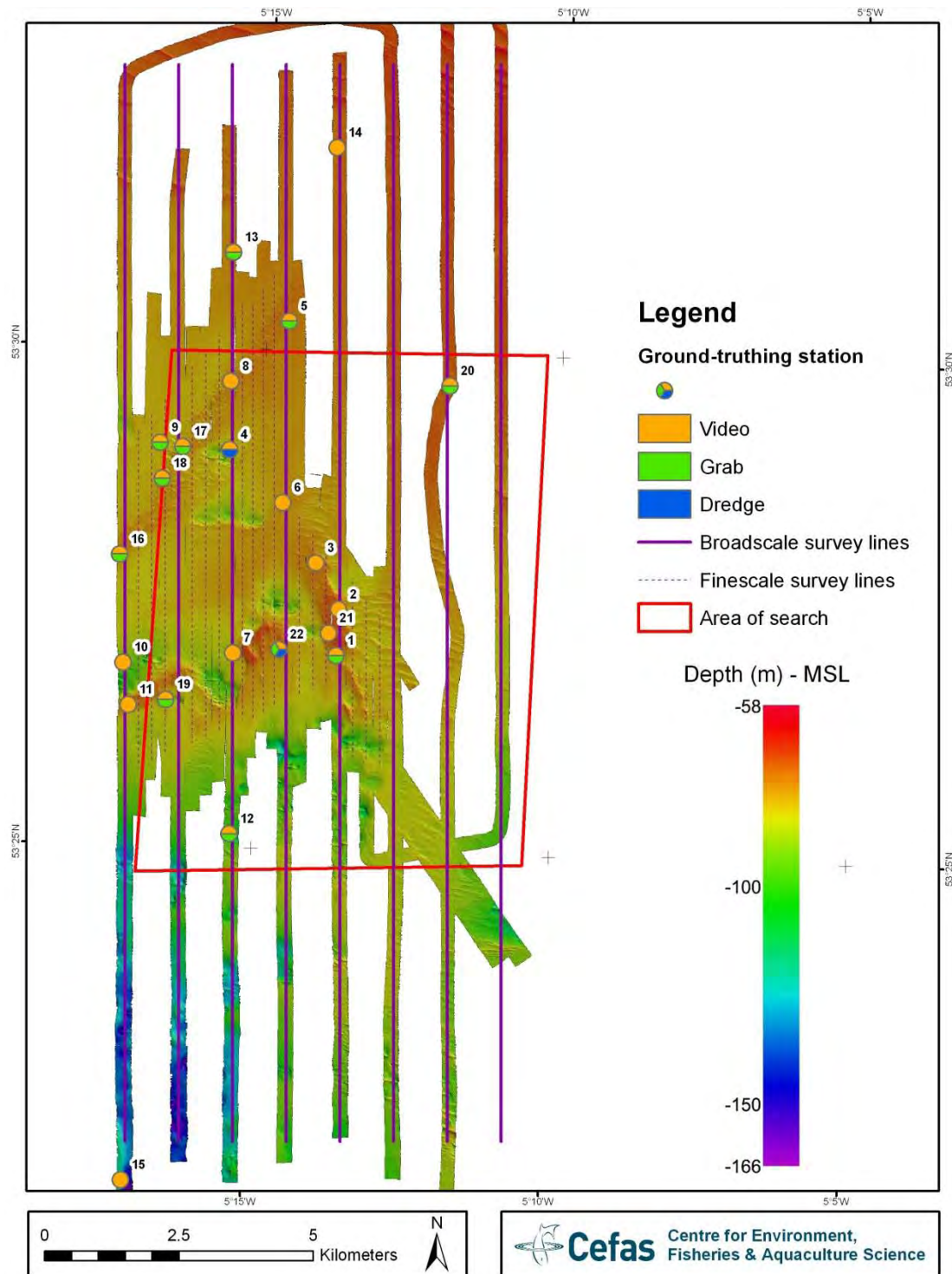


Figure 2. Summary diagram of survey lines and sampling points at Submarine Structures in the Mid Irish Sea area of study (taken from Whormersley *et al.*, 2008).

Geological background

The geological background of the study area is summarised by Whormersley *et al.* (2008). The study area is underlain by inclined strata of Carboniferous (Dinantian and Westphalian) age. These bedrocks have been weathered and form an irregular unconformity surface that is between 20 to 60 m below the seabed. Carboniferous strata

are overlain by the shallowly dipping or sub horizontal sediments of the Quaternary Prograded Facies of the Western Irish Sea Formation, formed during deglaciation of the Irish Sea after the last glacial maximum. The Quaternary sediments are themselves cut by several trenches and scarps that are presumed by Whormersley *et al.* (2008) to be related to ongoing erosion at the sea floor by tidal currents, possibly augmented by gas escape at the seabed.

A thin veneer of gravely sand containing shell fragments covers much of the study area. This is the active layer being mobilised at the seabed in the current hydrological regime. Larger sediment wave forms are present in the area, with crests running east-west for up to 1 km, but these may not be active. MDAC has been identified beneath the active layer, and may be exposed and undercut by seabed erosion.

Analytical methods

3.1 Petrographical analysis

3.1.1 Polished section and polished block preparation

Polished thin sections for petrographical analysis were prepared from small blocks, approximately 40 x 25 x 15 mm, that were sawn from the MDAC samples. The blocks were impregnated with epoxy-resin under vacuum in order to stabilise the material for polished section preparation. A blue dye was added to the epoxy-resin prior to vacuum impregnation to differentiate between porosity originally present within sample and any artefacts of the sectioning process (e.g. grain plucking), when subsequently observed by transmitted-light microscopy. These resin-impregnated blocks were then sliced, and the slice polished to produce polished thin sections 30 µm thick bonded onto 45 x 28 mm glass microscope slides with a colourless epoxy-resin. The thin sections were finished by polishing with 0.45 µm diamond paste.

The residual counterpart resin-impregnated block to each thin section slice was also polished. This block was then used for microsampling by microdrilling, for stable isotope analysis as described in Section 3.3.

3.1.2 Optical microscopy

The polished thin sections and polished blocks were initially scanned, using a digital flatbed scanner, to provide reference images of the whole section/block area. The polished sections were then examined and photographed in transmitted light using a Zeiss Axioplan 2 petrological (polarising) microscope, fitted with a digital camera.

3.1.3 Cathodoluminescence microscopy

The polished blocks were examined by cathodoluminescence (CL) microscopy in order to differentiate different types and generations of carbonate cement, and the location of bioclastic carbonate detritus, on the basis of variations in luminescence characteristics. Mineralogical variations and subtle differences in minor and trace element chemistry within carbonate minerals can produce significant differences in luminescence characteristics when the mineral is irradiated with electrons (Marshall, 1988). In particular, this luminescence microscopy technique is very sensitive to small variations in Fe- and Mn- content within calcite and dolomite, and is able to differentiate growth zoning and different mineral generations within these carbonate mineral cements.

CL analysis was performed using a Technosyn Model 8200 Mark II cold-cathode cathodoluminoscope stage mounted on a Nikon transmitted optical microscope, fitted with long working distance objective lenses. Images were captured using a Nikon Coolpix 4500 digital camera.

3.1.4 Scanning electron microscopy and electron probe microanalysis

Backscattered scanning electron microscopy (BSEM) was used to make high-resolution petrographical observations of the polished thin sections. Image brightness in BSEM images is related to the average atomic number of the phases observed (Goldstein *et al.*, 1981), and this therefore allows differentiation of the minerals observed in polished sections on the basis of the image brightness. Prior to BSEM examination, the polished

surface of the thin section was made electrically conductive by coating with a thin layer of carbon (250Å thick) by vacuum evaporation of carbon.

The morphological characteristics of the intergranular carbonate cements in the MDAC samples was also examined by scanning electron microscopy (SEM) using secondary electron imaging (SEI). Freshly fractured MDAC material was prepared for SEM analysis by mounting small chips (approximately 10 mm³) onto 10 mm diameter pin-type aluminium SEM stub mounts, using Leit CCC™ conductive carbon cement. The stub-mounted samples were then carbon-coated prior to examination in the SEM instrument.

SEM and BSEM analyses were carried out using a LEO 435VP variable pressure digital scanning electron microscope fitted with a solid-state 4-element (diode) backscattered electron detector, and equipped with an Oxford Instruments INCA EDXA system with a thin window Si-Li X-ray detector capable of detecting elements from boron to uranium. The scanning electron microscope instrument was operated in the conventional high vacuum mode (<1 x 10⁻⁴ torr), using a 10-20 kV electron beam accelerating potential, beam currents between 200-800 pA, and a working distance of 17-20 mm, as required. Mineral/phase identification was aided by microchemical information obtained from simultaneous observation of semi-quantitative EDXA spectra recorded from features of interest.

Quantitative electron probe microanalysis of the carbonate cements observed in polished thin section was also undertaken by SEM-EDXA. Quantitative EDXA electron probe microanalyses were performed using a 20 kV electron beam, 200-400 pA beam currents and at a working distance of 19 mm. Recorded EDXA spectra were processed and quantified using the INCA Suite Version 4.08 (2006) standard-less analysis software package, using a cobalt internal reference to calibrate instrument drift.

3.2 X-ray diffraction analysis

Whole rock X-ray diffraction (XRD) analysis was undertaken on 2 samples – ST 27 G22 and ST36 RD04 –to confirm the identification of the carbonate cements observed during petrographical analysis. For XRD analysis, approximately 10 mm³ lumps of the rock were ground in pestle and mortar and a c.3 g portion of the ground material was then wet-micronised under acetone for 10 minutes, dried, disaggregated and back-loaded into standard stainless steel sample holders to prepare random-orientated powder mounts for analysis.

XRD analysis was carried out using a PANalytical X'Pert Pro series diffractometer equipped with a cobalt-target tube, X'Celerator detector and operated at 45 kV and 40 mA. The random powder mounts were scanned from 4.5-55 °2θ at 2.76 °2θ/minute. Diffraction data were initially analysed using PANalytical X'Pert Highscore Plus version 2.2a software coupled to the latest version of the International Centre for Diffraction Data (ICDD) database.

3.3 Stable isotope analysis

Thirty sub-samples of MDAC were analysed to determine oxygen and carbon stable isotope (δ¹⁸O and δ¹³C) composition of the carbonate components. These included a bulk sample and three to five subsamples recovered by microsampling discrete areas of the

polished blocks that contained (or were dominated by) specific generations or types of carbonate (including bioclasts and cement types). The areas for microsampling were identified from optical and cathodoluminescence microscopy carried out previously on the resin impregnated polished blocks. This methodology has been very successfully used in previous studies to sample and analyse discrete generations of carbonate mineralisation in intergrown polymineralic or multi-generation carbonate cements (Milodowski *et al.*, 2005).

Microsampling was undertaken using a diamond-tipped microdrill, whilst observing the block sample in reflected light under an optical microscope. The microdrill was capable of drilling and recovering material from areas as small as 100 μm . However, in order to obtain sufficient material for analysis areas up to 1 mm diameter were drilled.

An automated common acid bath VG Isocarb + Optima mass spectrometer was used to analyse approximately 60 mg of powder from each calcite subsample. Isotope values ($\delta^{13}\text{C}$, $\delta^{18}\text{O}$) are reported as per mil (‰) deviations of the isotopic ratios ($^{13}\text{C}/^{12}\text{C}$, $^{18}\text{O}/^{16}\text{O}$) calculated to the Pee Dee Belemnite (PDB) international reference (*via* a 'Virtual Pee Dee Belemnite' [VPDB] international standard that is referenced back to the original PDB standard), and the Standard Mean Ocean Water (SMOW) scales using an internal laboratory standard, calibrated against NBS standards, that is analysed along with the samples. Analytical reproducibility is typically $<0.1\%$ for both $\delta^{13}\text{C}$ and $\delta^{18}\text{O}$ (based on similarly sized laboratory standards).

Mineralogy and petrography

4.1. Sample ST12 Sledge

Sample ST12 Sledge comprises moderately-sorted medium sandstone, ranging in grain size from silt and very fine sand to coarse sand. The sand grains are dominantly rounded and sub-rounded with a minor amount of more angular silt to very fine sand. Some sand grains appear to be very well rounded aeolian grains. The sand is composed dominantly of detrital quartz, with minor plagioclase, K-feldspar, lithic clasts (including silicified siltstone, chert, altered fine grained igneous rock and limestone clasts) and calcareous bioclastic detritus (including fragments of bivalve and gastropod shells, multi-chambered foraminiferal tests and unidentified stellate and “wheel-shaped” spicules). Pelloidal grains composed of fine detrital clay (illitic, chloritic) are also present and may represent faecal pellets.

The sand typically displays an uncompacted grain fabric partially supported by a muddy and or micritic carbonate matrix or cement. The rock has a rubbly outer crust, encrusted by calcareous worm tubes, and internally is cut by large sub-horizontal burrow structures, up to 5 mm diameter channels up to 5 mm which are maintained as open channels by carbonate cementation of the adjacent sediment matrix.

The rock is patchily cemented by carbonate cement, with irregular sub-horizontal layers of sand tightly-cemented by micritic to microsparry calcium carbonate and layers of friable to weakly-cemented sand with abundant intergranular porosity. Some lithic grains are altered with intragranular microporosity produced as a

Four distinct generations or types of calcium carbonate cement fabric can be identified:

1. A fine isopachous calcium carbonate forming thin fringes up to 10 μm thick nucleated directly on top of detrital sand grains (Plate 1). It consists of fibrous or acicular crystals that have grown perpendicular to the grain surface. This is the earliest generation of cement.
2. Very fine microsparry to micritic calcium carbonate cement, that often appears brownish due to the presence of traces of very finely disseminated iron oxyhydroxide. The crystal size is often less than 2 μm but may be partially recrystallised or locally coarsened to form crystals up to 10 μm diameter This encloses the earlier isopachous grain fringing carbonate cement (Plate 1).
3. Late-stage acicular crystals lining open intergranular pores (Plate 1 and Plate 2). These have a flattened orthorhombic needle to bladed crystal morphology, consistent with the crystal forms of aragonite. Where the micrite or microsparry calcium carbonate is absent, these aragonite needles can be seen nucleated directly on top of the earlier isopachous grain-fringing cement or form as acicular coatings on top of bioclastic fragments (Plate 3) or encrusting clay pellets (Plate 4).
4. Pelloidal or microbotryoidal carbonate grains (Plate 1 and Plate 2). These are composed of fine micritic to microsparry calcium carbonate that are delineated in thin section by iron oxide staining (Plate 1), often with a darker outer fringe of brown iron oxyhydroxide. In many cases the pelloidal carbonate is semi-opaque in thin section, with pelloid sizes similar to the detrital quartz (Plate 2), and they may represent carbonate sediment reworked biologically as faecal pellets. However, many of the pelloidal or microbotryoidal grains are somewhat finer than the

detrital quartz and appear to have grown in situ within the intergranular porosity. The pelloidal grains can be seen to be composed of subsequent, euhedral crystals of calcium carbonate up to 10 μm diameter (Plate 5).

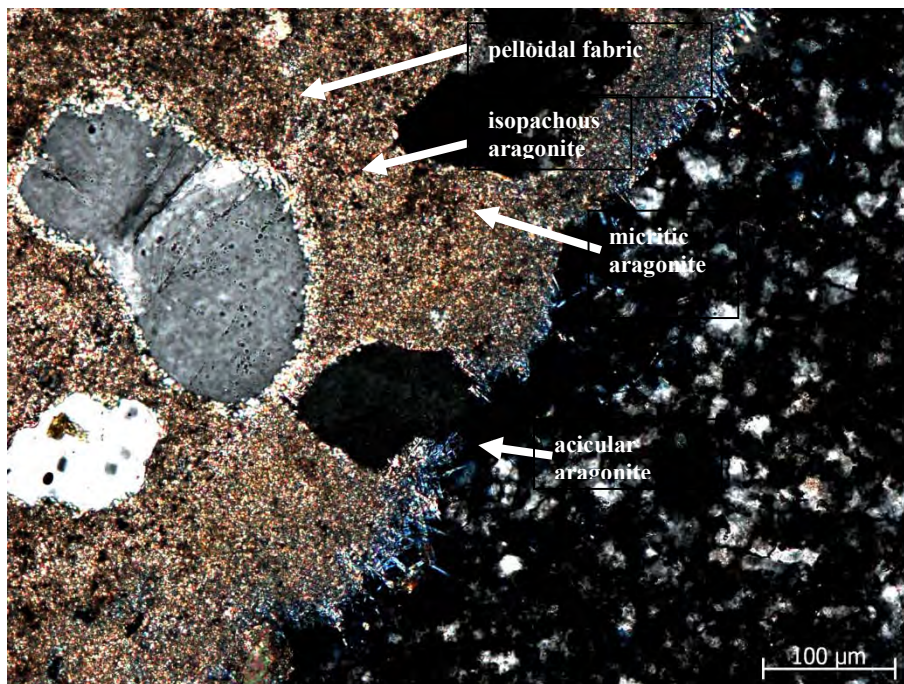


Plate 1. Transmitted light photomicrograph (crossed polars) at the interface between a densely-carbonate cemented (birefringent area) and porous weakly cemented (dark area) MDAC sandstone. The rock has a very open quartz grain fabric, and displays three generations of carbonate cement: (1) early isopachous grain-fringing aragonite, enclosed beneath; (2) dense micritic or microsparry aragonite, and; (3) later acicular (needles) aragonite lining open pores. Sample ST12 Sledge.

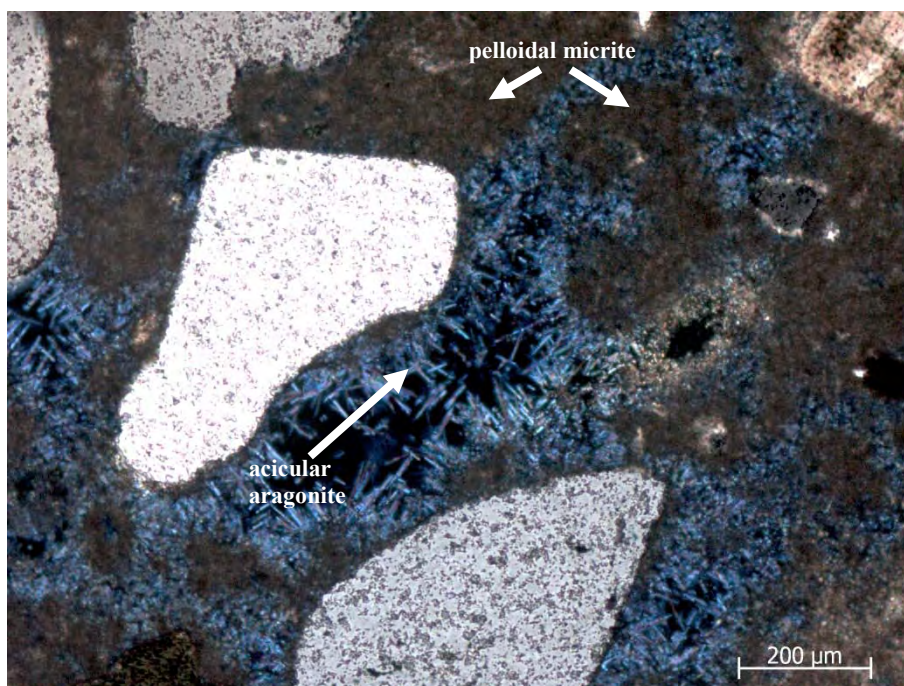


Plate 2. Transmitted light photomicrograph (crossed polars) showing abundant disseminated brownish fine sand- to silt-grade botryoidal or pelloidal grains composed of

fine grained birefringent aragonite and fine-to medium sand-grade quartz (white), encrusted with acicular (needles) aragonite lining open porosity (black). Sample ST12 Sledge.

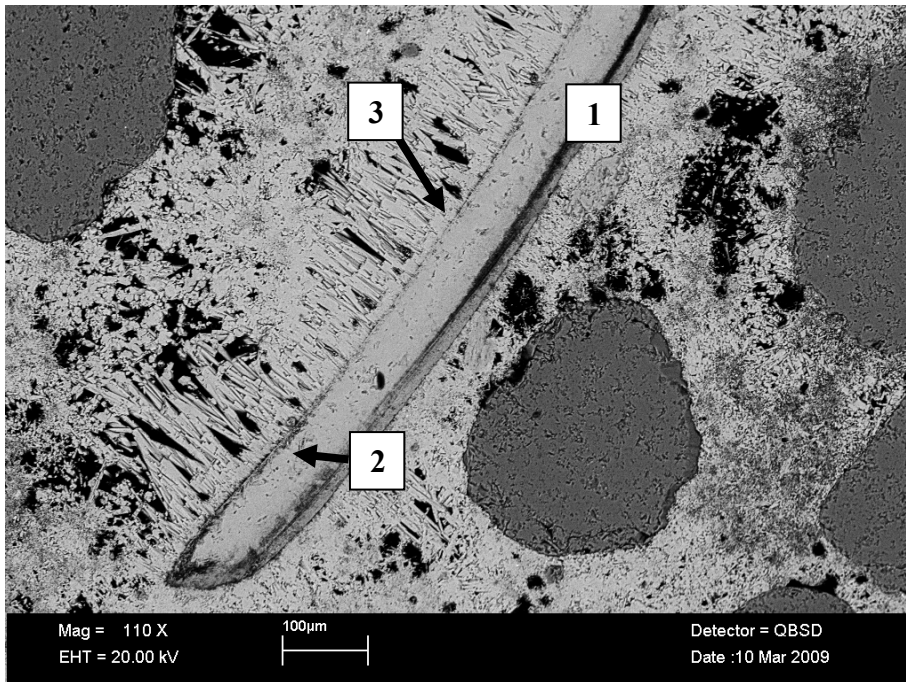


Plate 3. BSE image showing a fragment of bivalve shell (1), coated with very thin isopachous aragonite fringe cement (2) from which later acicular aragonite cement (3) has nucleated. Sample ST12 Sledge.

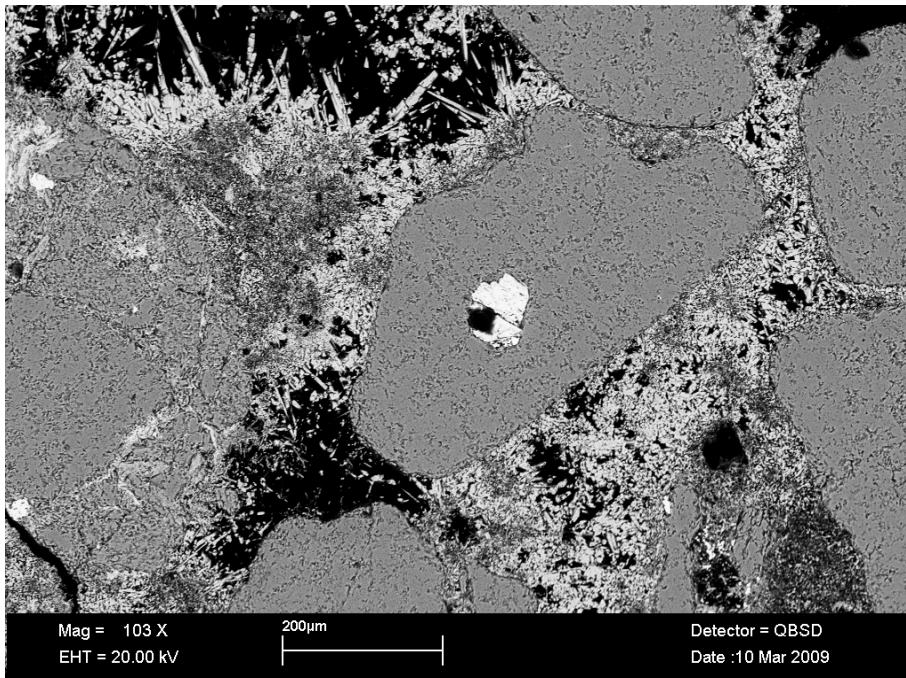


Plate 4. BSE image showing the growth of needles of aragonite into open intergranular pores. The aragonite has nucleated on the surface of clay-rich "pellets" or "clots" or grain-coating clay pellicles (fine dark grey material). Sample ST12 Sledge.

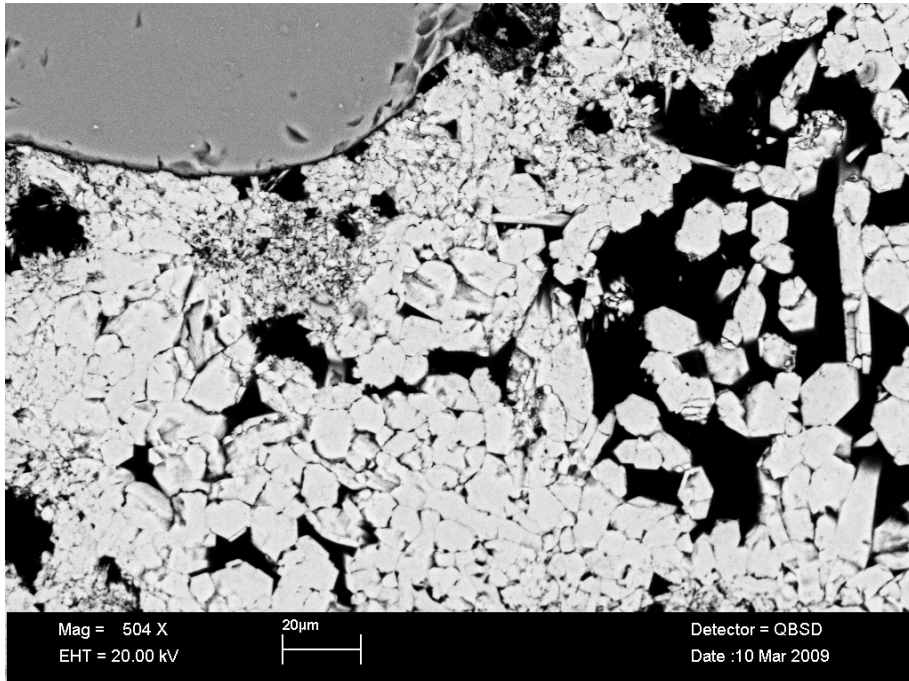


Plate 5. BSEM image showing the tightly-interlocking microcrystalline fabric of the “clots” or “pellets” of aragonite that form the locally densely-cemented domains of MDAC sandstone. In more open pore space, the aragonite develops equant euhedral crystal form. Sample ST12 Sledge.

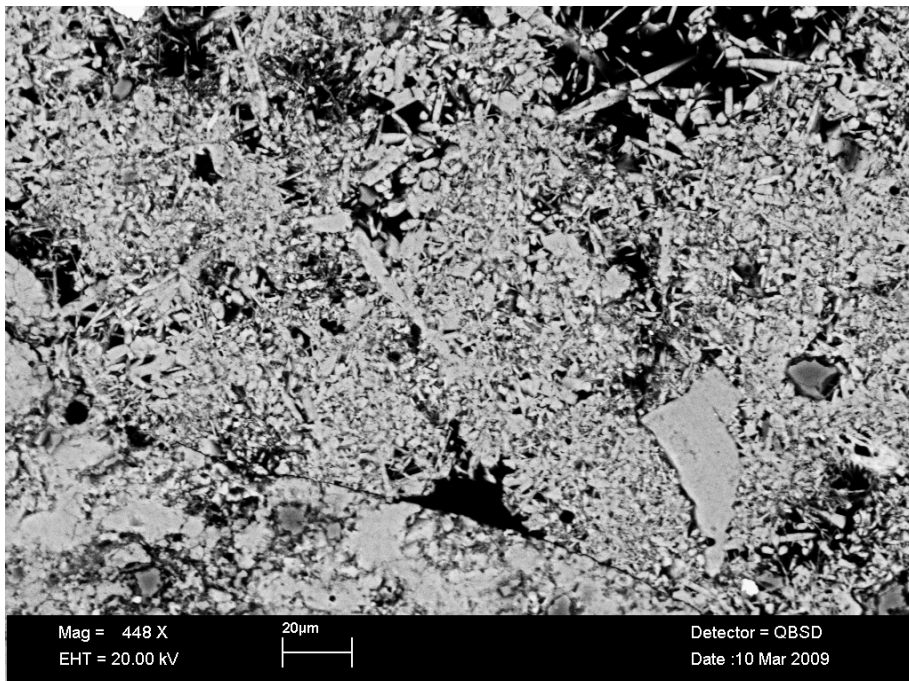


Plate 6. BSEM image displaying the tightly-interlocking micritic microcrystalline fabric of the “clots” or “pellets” of aragonite that form the locally densely-cemented domains of MDAC sandstone. Aragonite nucleated on the surfaces of these “pellets” has grown as needles into the open pores. Sample ST12 Sledge.

Areas of tightly cemented sandstone often appear to consist of a matrix of abundant partially recrystallised and tightly cemented carbonate pelloids containing disseminated detrital clay and clay-rich pellets (Plate 6).

Electron microprobe analyses from the carbonate cements in sample ST12 Sledge are given in Table 14 and their compositional variation, expressed in terms of molar proportions of CaCO_3 - MgCO_3 - SrCO_3 , is summarised in Figure 59. All four types of carbonate have essentially the same chemical composition. They consist of calcium carbonate with 1 to 2 mole % SrCO_3 in solid solution. The relatively high Sr content suggests that all four types/generations of carbonate cement are aragonite rather than calcite, since Sr is much more abundant in aragonite than in calcite (Deer *et al.*, 1962). This is because Sr is much more readily incorporated in the orthorhombic crystal structure of aragonite, which can form a partial solid-solution series with the end-member orthorhombic strontianite (SrCO_3).

Aragonite cement has been recorded previously by Judd (2005) in MDAC from this area of the Mid Irish Sea, and needles of aragonite have also been described encrusting sand grains (similar to the late-stage acicular aragonite described above) by Croker *et al.* (2005) from SEM observations of very limited “anchor samples” recovered from potential MDAC in the Western Irish Sea. Similar acicular and “pelleted” or “botryoidal” aragonite fabrics have been observed in previous studies of MDAC from other areas (e.g. Hovland and Talbot, 1987; Jensen *et al.*, 1992; Bohrmann *et al.*, 1998; Peckmann *et al.*, 2001; Muralidhar *et al.*, 2006). Peckmann *et al.* (2001) report the formation of acicular Sr-rich aragonite cement, with between 8300-9500 ppm Sr, in MDAC associated with methane seeps from the Black Sea. The strontium content of the aragonite cements reported by Peckmann *et al.* (2001) is of a similar order of magnitude to those we describe from the Mid Irish Sea (Table 2, Figure 3).

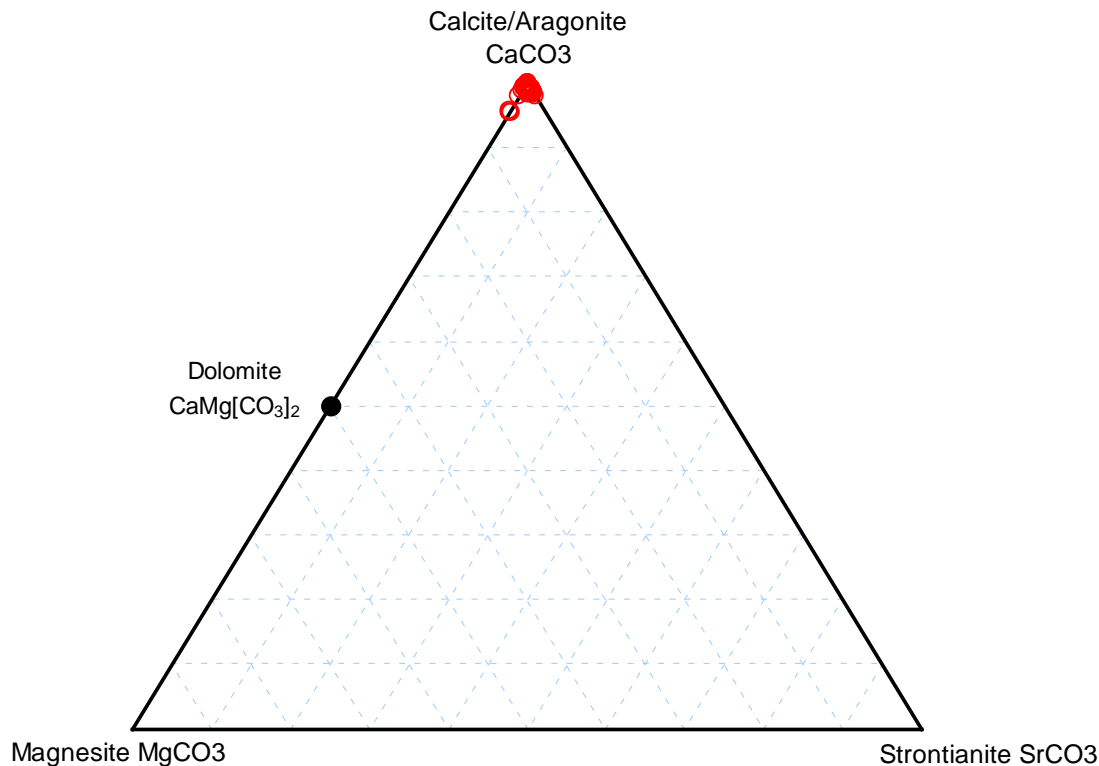


Figure 3. CaCO_3 - MgCO_3 - SrCO_3 molar ratio plot illustrating the composition of the aragonite cement in MDAC sample “ST12 Sledge”, relative to end-member carbonate minerals

Table 2. Electron microprobe of carbonate cements and other carbonate components in sample ST12 SLEDGE

No.	WEIGHT % OXIDE							IONIC RATIO [normalised to 3 [O]						COMMENTS
	MgO	CaO	MnO	FeO	SrO	CO ₂ (calc)	Total wt%	Mg ²⁺	Ca ²⁺	Mn ²⁺	Fe ²⁺	Sr ²⁺	CO ₃ ²⁻	
1	0.00	54.86	0.00	0.00	1.51	43.69	100.06	0.00	0.99	0.00	0.00	0.01	1.00	Acicular aragonite
2	0.00	55.46	0.00	0.00	1.32	44.08	100.87	0.00	0.99	0.00	0.00	0.01	1.00	Acicular aragonite
3	0.00	55.07	0.00	0.00	2.07	44.09	101.23	0.00	0.98	0.00	0.00	0.02	1.00	Acicular aragonite
4	0.00	55.76	0.00	0.00	1.34	44.31	101.41	0.00	0.99	0.00	0.00	0.01	1.00	Acicular aragonite
5	0.00	54.21	0.00	0.00	1.49	43.16	98.86	0.00	0.99	0.00	0.00	0.01	1.00	Acicular aragonite
6	0.00	55.35	0.00	0.00	1.75	44.17	101.28	0.00	0.98	0.00	0.00	0.02	1.00	Acicular aragonite
7	0.00	55.17	0.00	0.00	1.50	43.92	100.60	0.00	0.99	0.00	0.00	0.01	1.00	Acicular aragonite
8	0.00	55.93	0.00	0.00	1.23	44.40	101.56	0.00	0.99	0.00	0.00	0.01	1.00	Acicular aragonite
9	0.00	55.62	0.00	0.00	1.34	44.21	101.16	0.00	0.99	0.00	0.00	0.01	1.00	Acicular aragonite
10	0.00	55.76	0.00	0.00	1.34	44.31	101.41	0.00	0.99	0.00	0.00	0.01	1.00	Acicular aragonite
11	0.00	55.55	0.00	0.00	1.06	44.03	100.65	0.00	0.99	0.00	0.00	0.01	1.00	Acicular aragonite
12	0.00	55.13	0.00	0.00	1.04	43.70	99.86	0.00	0.99	0.00	0.00	0.01	1.00	Acicular aragonite
13	0.00	55.72	0.00	0.00	1.60	44.39	101.71	0.00	0.98	0.00	0.00	0.02	1.00	Acicular aragonite
14	0.00	55.09	0.00	0.00	1.32	43.78	100.19	0.00	0.99	0.00	0.00	0.01	1.00	Acicular aragonite
15	0.00	55.17	0.00	0.00	1.12	43.76	100.06	0.00	0.99	0.00	0.00	0.01	1.00	Pelletised microgranular matrix aragonite closely associated with acicular aragonite cement
16	0.00	54.58	0.00	0.00	1.27	43.36	99.21	0.00	0.99	0.00	0.00	0.01	1.00	Pelletised microgranular matrix aragonite closely associated with acicular aragonite cement
17	0.00	54.95	0.00	0.00	1.67	43.82	100.43	0.00	0.98	0.00	0.00	0.02	1.00	Pelletised microgranular matrix aragonite closely associated with acicular aragonite cement
18	0.00	54.41	0.00	0.00	1.45	43.31	99.18	0.00	0.99	0.00	0.00	0.01	1.00	Pelletised microgranular matrix aragonite closely associated with acicular aragonite cement
19	0.00	53.95	0.00	0.00	1.17	42.83	97.95	0.00	0.99	0.00	0.00	0.01	1.00	Pelletised microgranular matrix aragonite closely associated with acicular aragonite cement

No.	WEIGHT % OXIDE							IONIC RATIO [normalised to 3 [O]						COMMENTS
	MgO	CaO	MnO	FeO	SrO	CO ₂ (calc)	Total wt%	Mg ²⁺	Ca ²⁺	Mn ²⁺	Fe ²⁺	Sr ²⁺	CO ₃ ²⁻	
20	0.00	54.88	0.00	0.00	1.24	43.58	99.70	0.00	0.99	0.00	0.00	0.01	1.00	Fine microspar aragonite forming tight intergranular cement
21	0.00	55.14	0.00	0.00	1.11	43.74	99.99	0.00	0.99	0.00	0.00	0.01	1.00	Fine microspar aragonite forming tight intergranular cement
22	0.00	55.84	0.00	0.00	1.08	44.27	101.19	0.00	0.99	0.00	0.00	0.01	1.00	Fine microspar aragonite forming tight intergranular cement
23	0.00	55.34	0.00	0.00	1.48	44.05	100.86	0.00	0.99	0.00	0.00	0.01	1.00	Fine microspar aragonite forming tight intergranular cement
24	0.00	55.06	0.00	0.00	1.43	43.81	100.30	0.00	0.99	0.00	0.00	0.01	1.00	Fine microspar aragonite forming tight intergranular cement
25	0.00	54.96	0.00	0.00	1.12	43.60	99.68	0.00	0.99	0.00	0.00	0.01	1.00	Fine microspar aragonite forming tight intergranular cement
26	0.00	54.75	0.00	0.00	1.03	43.39	99.17	0.00	0.99	0.00	0.00	0.01	1.00	Fine microspar aragonite forming tight intergranular cement
27	0.00	54.75	0.00	0.00	0.72	43.26	98.74	0.00	0.99	0.00	0.00	0.01	1.00	Microspar aragonite cement filling between acicular aragonite cement
28	0.20	55.38	0.00	0.00	0.90	44.05	100.53	0.00	0.99	0.00	0.00	0.01	1.00	Microspar aragonite cement filling between acicular aragonite cement
29	0.33	54.36	0.00	0.00	1.06	43.46	99.22	0.01	0.98	0.00	0.00	0.01	1.00	Microspar aragonite cement filling between acicular aragonite cement
30	0.00	54.78	0.00	0.00	0.95	43.38	99.11	0.00	0.99	0.00	0.00	0.01	1.00	Microspar aragonite cement filling between acicular aragonite cement
31	0.00	54.83	0.00	0.00	0.93	43.42	99.19	0.00	0.99	0.00	0.00	0.01	1.00	Microspar aragonite cement filling between acicular aragonite cement
32	0.00	55.31	0.00	0.00	0.82	43.74	99.87	0.00	0.99	0.00	0.00	0.01	1.00	Coarser equant aragonite filling between acicular calcium carbonate cement
33	0.00	54.47	0.00	0.00	0.69	43.03	98.19	0.00	0.99	0.00	0.00	0.01	1.00	Coarser equant aragonite filling between acicular calcium carbonate cement
34	0.00	55.20	0.00	0.00	1.08	43.77	100.04	0.00	0.99	0.00	0.00	0.01	1.00	Coarser equant aragonite filling between acicular calcium carbonate cement

No.	WEIGHT % OXIDE							IONIC RATIO [normalised to 3 [O]						COMMENTS
	MgO	CaO	MnO	FeO	SrO	CO ₂ (calc)	Total wt%	Mg ²⁺	Ca ²⁺	Mn ²⁺	Fe ²⁺	Sr ²⁺	CO ₃ ²⁻	
35	0.00	54.67	0.00	0.00	0.86	43.26	98.79	0.00	0.99	0.00	0.00	0.01	1.00	Coarser equant aragonite filling between acicular calcium carbonate cement
36	0.00	54.67	0.00	0.00	0.65	43.17	98.48	0.00	0.99	0.00	0.00	0.01	1.00	Coarser equant aragonite filling between acicular calcium carbonate cement
37	0.00	52.23	0.00	0.00	0.65	41.26	94.14	0.00	0.99	0.00	0.00	0.01	1.00	Early fine micritic carbonate "clots" or spheroidal aggregates (low totals due to microporosity)
38	0.00	53.25	0.00	0.00	0.99	42.20	96.45	0.00	0.99	0.00	0.00	0.01	1.00	Early fine micritic carbonate "clots" or spheroidal aggregates (low totals due to microporosity)
39	0.00	53.59	0.00	0.00	0.64	42.32	96.55	0.00	0.99	0.00	0.00	0.01	1.00	Early fine micritic carbonate "clots" or spheroidal aggregates (low totals due to microporosity)
40	0.00	52.16	0.00	0.00	1.43	41.53	95.13	0.00	0.99	0.00	0.00	0.01	1.00	Microspar cement grown displacively within clay matrix
41	0.00	53.58	0.00	0.00	1.05	42.48	97.11	0.00	0.99	0.00	0.00	0.01	1.00	Microspar cement grown displacively within clay matrix
42	0.00	51.56	0.00	0.00	0.93	40.85	93.35	0.00	0.99	0.00	0.00	0.01	1.00	Microspar cement grown displacively within clay matrix
43	0.35	53.39	0.00	0.00	0.00	42.27	96.01	0.01	0.99	0.00	0.00	0.00	1.00	Microspar cement grown displacively within clay matrix
44	0.30	55.51	0.18	0.00	0.00	43.99	99.97	0.01	0.99	0.00	0.00	0.00	1.00	Detrital limestone clast
45	0.50	54.41	0.00	0.00	0.00	43.24	98.15	0.01	0.99	0.00	0.00	0.00	1.00	Detrital limestone clast
46	0.00	54.53	0.00	0.00	0.00	42.78	97.31	0.00	1.00	0.00	0.00	0.00	1.00	Detrital limestone clast
47	1.67	53.59	0.00	0.00	0.39	44.04	99.69	0.04	0.95	0.00	0.00	0.00	1.00	Bioclastic material - foraminiferal test
48	1.72	52.69	0.00	0.00	0.00	43.23	97.64	0.04	0.96	0.00	0.00	0.00	1.00	Bioclastic material - foraminiferal test
49	1.81	53.00	0.00	0.00	0.00	43.56	98.37	0.05	0.95	0.00	0.00	0.00	1.00	Bioclastic material - foraminiferal test
50	0.78	53.95	0.00	0.00	0.00	43.18	97.91	0.02	0.98	0.00	0.00	0.00	1.00	Bioclastic material - foraminiferal test
51	0.30	54.88	0.00	0.00	0.00	43.38	98.56	0.01	0.99	0.00	0.00	0.00	1.00	Bioclastic material - foraminiferal test
52	0.00	54.62	0.00	0.00	0.30	42.98	97.90	0.00	1.00	0.00	0.00	0.00	1.00	Bioclastic material - bivalve shell fragment

No.	WEIGHT % OXIDE							IONIC RATIO [normalised to 3 [O]						COMMENTS
	MgO	CaO	MnO	FeO	SrO	CO ₂ (calc)	Total wt%	Mg ²⁺	Ca ²⁺	Mn ²⁺	Fe ²⁺	Sr ²⁺	CO ₃ ²⁻	
53	0.00	54.89	0.00	0.00	0.00	43.07	97.96	0.00	1.00	0.00	0.00	0.00	1.00	Bioclastic material - bivalve shell fragment
54	0.00	55.25	0.00	0.00	0.00	43.35	98.61	0.00	1.00	0.00	0.00	0.00	1.00	Bioclastic material - bivalve shell fragment
55	0.20	54.48	0.00	0.00	0.30	43.09	98.07	0.01	0.99	0.00	0.00	0.00	1.00	Bioclastic material - bivalve shell fragment
56	0.18	54.48	0.00	0.00	0.00	42.95	97.61	0.00	1.00	0.00	0.00	0.00	1.00	Bioclastic material - bivalve shell fragment

Sample ST21 G09

Sample ST21 G09 comprises moderately-sorted fine to medium sandstone, ranging in grain size from silt and very fine sand to coarse sand. The sand grains are dominantly angular to sub-angular grains (Plate 7). The sand is composed dominantly of detrital quartz, with minor plagioclase, K-feldspar, lithic clasts (including siltstone, chert, and limestone clasts) and calcareous bioclastic detritus (including abraded fragments of mollusc shells and multi-chambered foraminiferal tests). Well-rounded grains of fresh green glauconite are also present (Plate 8) as an accessory component.

The rock is colour-banded with the outer margins oxidised and stained light brown by disseminated fine grain iron oxyhydroxides to a depth of 3-5 mm. Beneath this, the interior of the sample is a fresh light grey green colour. The rock appears to have been significantly bioturbated, with evidence of small irregular sub-horizontal burrow structures connecting with short (3-5 mm long) vertical burrows. The outer surface of the sandstone also contains borings.

Most of the carbonate cement binding the sandstone comprises very fine micritic or microcrystalline dolomite (dolomicrite), which is often nearly opaque in thin section or heavily coloured brown due to the presence of very fine disseminated iron oxides or oxyhydroxides (Plate 8). An early isopachous grain-coating rim of fine grained dolomite (similar to the early isopachous aragonite cement seen in sample ST12 Sledge) may sometimes be preserved beneath the micritic dolomite matrix (Plate 9). Much of this matrix carbonate appears to be formed by closely-packed pelloids or “clots” of micrite that have coalesced and “merged” to produce a dense micritic matrix. Some of this occurs as a very patchy intergranular matrix that in places appears to represent diffuse burrow infills and may be of faecal origin.

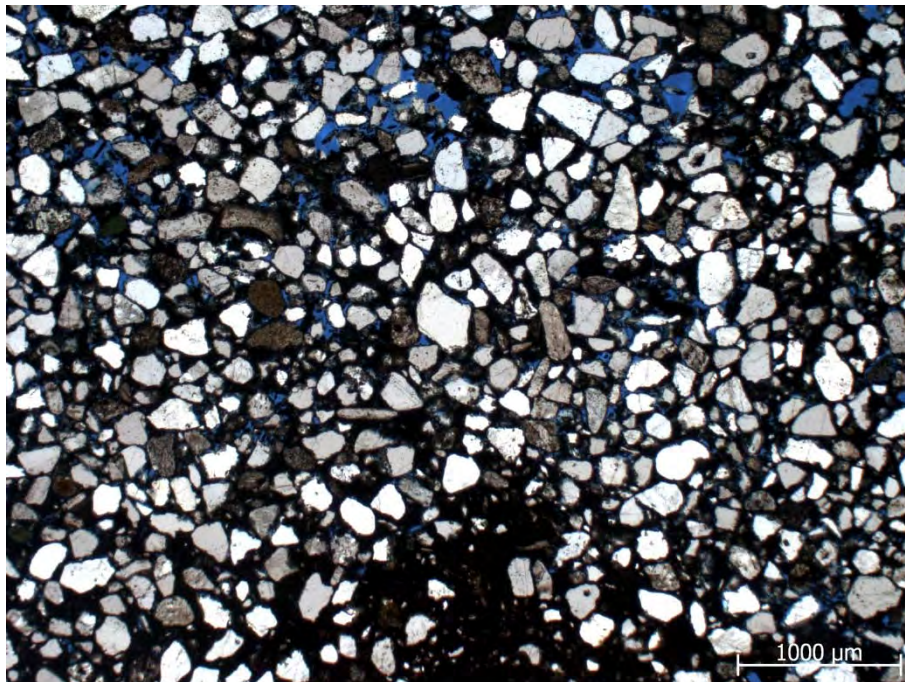


Plate 7. Transmitted light photomicrograph (plane-polarised light) showing moderately-sorted, very fine to medium sandstone, composed of dominantly of angular detrital quartz grains (clear) and subordinate detrital K-feldspar and plagioclase (cloudy grains). [The

rock is cemented by fine-grained, patchy micritic dolomite that appears dark brown to semi-opaque due to staining with disseminated fine iron oxide. Sample ST21 G09.

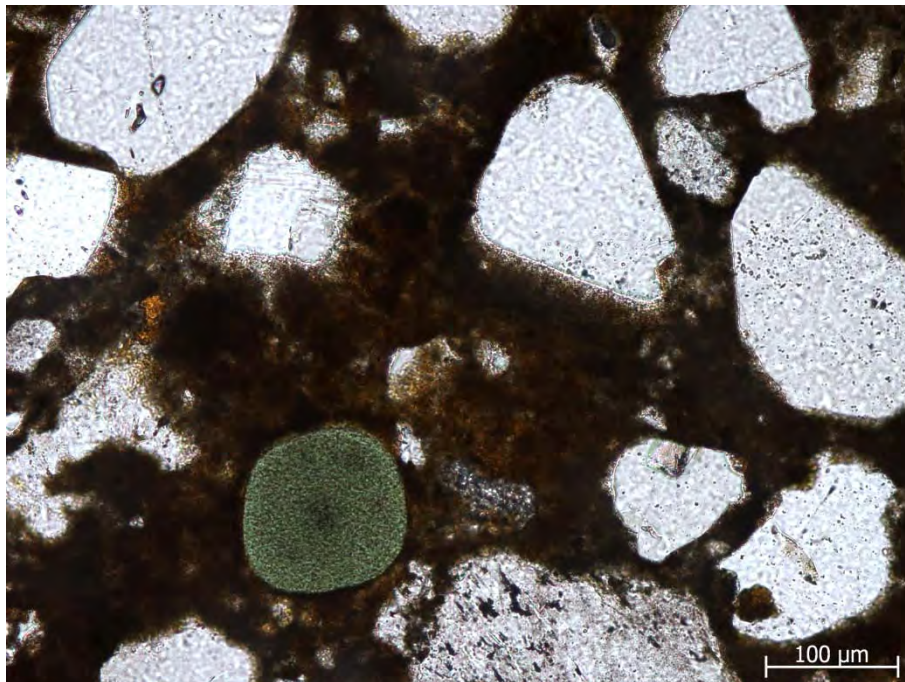


Plate 8. Transmitted light photomicrograph (plane-polarised light) showing sub-angular and sub-rounded detrital quartz (clear) and partially altered feldspar (cloudy) sand grains. A well-rounded grain of fresh glauconite (green) is also seen. Fine-grained, brown to semi-opaque dolomicrite forms the intergranular matrix and also forms a “pelloidal” fabric that appears to have a similar grain size to the quartz sand grains. Sample ST21 G09.

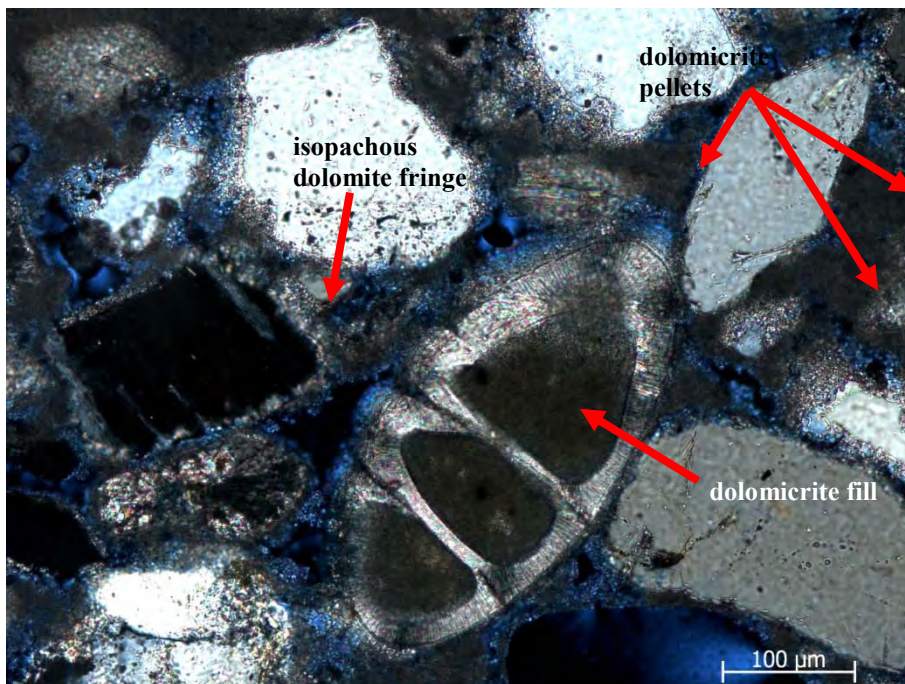


Plate 9. Transmitted light photomicrograph (crossed-polars) showing angular detrital quartz and a well-preserved calcareous multi-chambered foraminiferal test. The detrital grains are bonded by highly birefringence isopachous fine-grained dolomite cement forming a grain-coating fringe or meniscus. Fine-grained, semi-opaque dolomicrite fills

the foraminiferal chambers and occurs as irregular patches and “silt-grade pellets in the matrix. Sample ST21 G09.

A high proportion of the pelleted or microbotryoidal micritic dolomite aggregates are much finer than the detrital quartz, and also fill the voids within chambered foraminiferal tests (Plate 9). BSEM observations show that the dolomite cement comprises spherical to framboidal (microbotryoidal) aggregates up to 30 μm diameter (Plate 10 and Plate 11), composed of very fine (1 to 2 μm) subidiomorphic to idiomorphic rhombic dolomite crystals lining the intergranular porosity. These pelloidal carbonate fabrics appear to have grown in situ, and are very similar to the aragonitic and high-magnesium calcite cements observed in sample ST12 Sledge and from MDAC described from methane seeps elsewhere (*cf.* Peckmann *et al.*, 2001; Muradlihar *et al.*, 2006). Under higher magnification, BSEM shows that the spheroidal or framboidal aggregates sometimes have hollow cores (Plate 12) around which the dolomite crystals appear to have nucleated. The cavities are typically of the order of 1 to 2 μm diameter. This is about the size of bacterial cells, and possibly these hollow cores might represent bacterial cells around which the carbonate mineralisation may have nucleated.

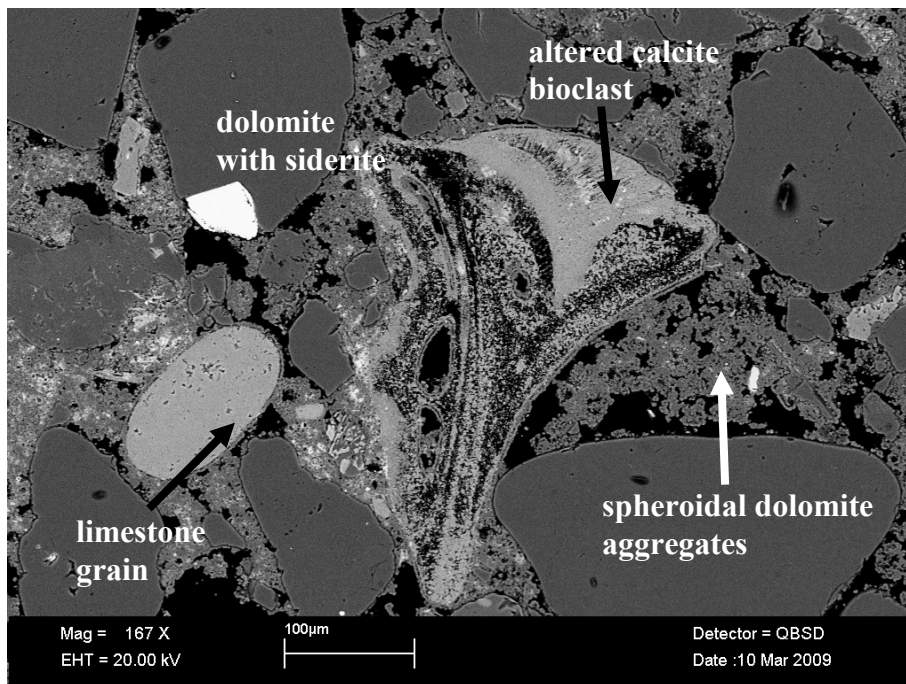


Plate 10. BSEM image showing clusters of microspheroidal aggregates of dolomite forming locally porous intergranular cement. Denser areas of dolomite cement are partially cemented or replaced by later siderite (bright) filling micropores in the dolomite cement. Sample ST21 G09.

Electron microprobe analyses of the dolomite cement are presented in Table 3. These data are summarised in Figure 60 in terms of molar proportions of end-member CaCO_3 - MgCO_3 - FeCO_3 . Figure 60 shows that the dolomite is calcium-rich, with up to 8 mole% Ca (average composition $\text{Ca}_{0.54}\text{Mg}_{0.46}\text{CO}_3$) in excess of the ideal stoichiometry for dolomite $\text{Ca}_{0.5}\text{Mg}_{0.5}\text{CO}_3$. This is very similar to the excess Ca dolomites (average composition $\text{Ca}_{0.53}\text{Mg}_{0.47}\text{CO}_3$) described by Jensen *et al.* (1992) from MDAC deposits in the Kattegat off the coast of Denmark. The presence of a significant excess in Ca in dolomite at low temperature may indicate that the dolomite is relatively poorly ordered and/or metastable,

and may have precipitated rapidly (Vahrenkamp and Swart, 1994) possibly forming via a “protodolomite” precursor (*cf.* Deer *et al.*, 1992).

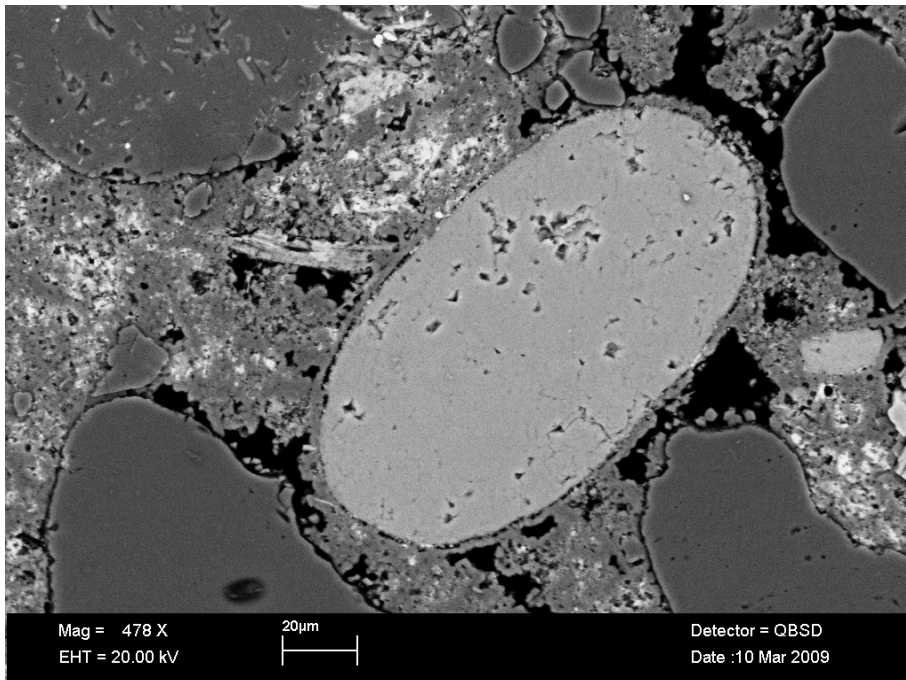


Plate 11. BSEM image showing rounded limestone grain (centre) with early isopachous dolomite fringe cement. The interstitial matrix is partially cemented by spheroidal clusters of fine microporous dolomite in which siderite (bright) partially fills the microporosity. Sample ST21 G09.

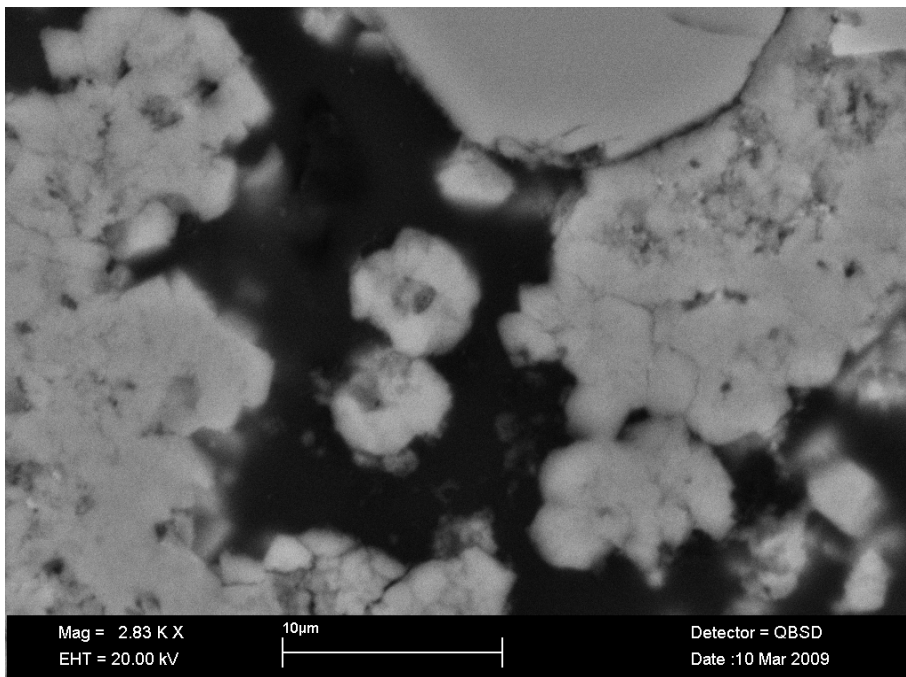


Plate 12. BSEM image showing detail of the microfabric of the microporous dolomite cement. The dolomite consists of “framboidal” aggregates of rhombic dolomite microcrystals, often nucleated around a “hollow core”. Sample ST21 G09.

In addition to dolomite, siderite was also identified within the carbonate cement. The siderite is very fine grained, occurring as thin overgrowths on the dolomite crystals, or filling micropores within the dolomitic pelloids (Plate 10 and Plate 11). Siderite does not appear to have been described from other MDAC (e.g. Hovland and Talbot, 1987; Jensen *et al.*, 1992; Bohrmann *et al.*, 1998; Peckmann *et al.*, 2001; Judd, 2005; Muralidhar *et al.*, 2006). Its formation in shallow marine sediments where bacterial reduction of sulphate might also be anticipated (e.g. Jensen *et al.*, 1992; Peckmann *et al.*, 2001; Muralidhar *et al.*, 2006) is enigmatic since any reduced iron (which is strongly chalcophilic) would be expected to preferentially precipitate as authigenic pyrite (or other iron sulphide).

Electron microprobe analyses of the siderite (Table 15 and Figure 60) give high analytical totals that significantly in excess of 100 wt% when calculated as carbonate (Table 15). This is because the siderite contains finely disseminated iron oxide that is unresolved in the analyses and results in an overestimate of FeCO_3 . Nevertheless, the data indicate that the siderite is magnesium-rich, with up to at least 11 mole % MgCO_3 in solid-solution. The presence of magnesium siderite is consistent with siderite formed in a marine environment (Mozley, 1989).

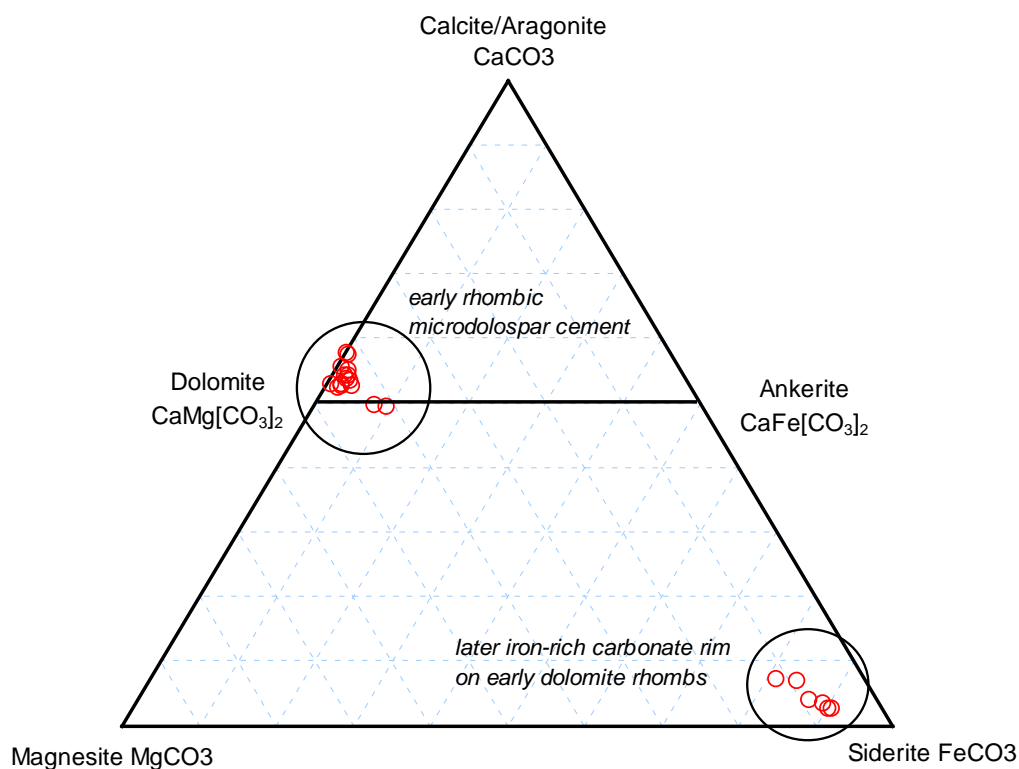


Figure 4. CaCO_3 - MgCO_3 - FeCO_3 molar ratio plot illustrating the composition of the carbonate cements in MDAC sample “ST21 G09”, relative to end-member carbonate minerals

Table 3. Electron microprobe of carbonate cements and other carbonate components in sample ST21 G09

No.	WEIGHT % OXIDE							IONIC RATIO [normalised to 3 [O]						COMMENTS
	MgO	CaO	MnO	FeO	SrO	CO ₂ (calc)	Total wt%	Mg ²⁺	Ca ²⁺	Mn ²⁺	Fe ²⁺	Sr ²⁺	CO ₃ ²⁻	
1	18.44	35.23	0.00	0.53	0.00	48.09	102.29	0.42	0.57	0.00	0.01	0.00	1.00	Early rhombic excess Ca-type microdolospar cement
2	18.21	34.85	0.00	0.39	0.00	47.46	100.90	0.42	0.58	0.00	0.00	0.00	1.00	Early rhombic excess Ca-type microdolospar cement
3	19.17	32.42	0.00	1.81	0.00	47.47	100.87	0.44	0.54	0.00	0.02	0.00	1.00	Early rhombic excess Ca-type microdolospar cement
4	18.77	32.07	0.00	1.43	0.00	46.52	98.79	0.44	0.54	0.00	0.02	0.00	1.00	Early rhombic excess Ca-type microdolospar cement
5	20.08	32.41	0.00	1.83	0.00	48.46	102.78	0.45	0.52	0.00	0.02	0.00	1.00	Early rhombic excess Ca-type microdolospar cement
6	18.69	31.69	0.00	2.25	0.00	46.64	99.27	0.44	0.53	0.00	0.03	0.00	1.00	Early rhombic excess Ca-type microdolospar cement
7	19.12	32.08	0.00	2.84	0.00	47.78	101.83	0.44	0.53	0.00	0.04	0.00	1.00	Early rhombic excess Ca-type microdolospar cement
8	17.56	29.54	0.00	7.36	0.00	46.85	101.30	0.41	0.49	0.00	0.10	0.00	1.00	Early rhombic excess Ca-type microdolospar cement
9	19.67	32.06	0.00	1.65	0.00	47.63	100.99	0.45	0.53	0.00	0.02	0.00	1.00	Early rhombic excess Ca-type microdolospar cement
10	18.44	30.05	0.00	6.21	0.00	47.51	102.22	0.42	0.50	0.00	0.08	0.00	1.00	Early rhombic excess Ca-type microdolospar cement
11	18.36	32.81	0.00	1.52	0.00	46.71	99.39	0.43	0.55	0.00	0.02	0.00	1.00	Dolomite fringe cement coating detrital grains
12	19.99	31.73	0.00	1.54	0.00	47.66	100.93	0.46	0.52	0.00	0.02	0.00	1.00	Dolomite fringe cement coating detrital grains
13	19.00	33.57	0.00	0.53	0.54	47.63	101.27	0.44	0.55	0.00	0.01	0.00	1.00	Dolomite fringe cement coating detrital grains
14	19.07	33.08	0.00	1.88	0.00	47.92	101.94	0.43	0.54	0.00	0.02	0.00	1.00	Dolomite fringe cement coating detrital grains
15	3.17	1.93	0.25	55.45	0.00	39.08	99.87	0.09	0.04	0.00	0.87	0.00	1.00	Siderite rim on early dolomite

No.	WEIGHT % OXIDE							IONIC RATIO [normalised to 3 [O]						COMMENTS
	MgO	CaO	MnO	FeO	SrO	CO ₂ (calc)	Total wt%	Mg ²⁺	Ca ²⁺	Mn ²⁺	Fe ²⁺	Sr ²⁺	CO ₃ ²⁻	
16	3.52	3.76	0.22	59.60	0.00	<i>43.43</i>	<i>110.53</i>	<i>0.09</i>	<i>0.07</i>	<i>0.00</i>	<i>0.84</i>	<i>0.00</i>	<i>1.00</i>	Siderite rim on early dolomite
17	4.68	4.11	0.22	59.05	0.00	<i>44.63</i>	<i>112.69</i>	<i>0.11</i>	<i>0.07</i>	<i>0.00</i>	<i>0.81</i>	<i>0.00</i>	<i>1.00</i>	Siderite rim on early dolomite
18	2.84	1.48	0.25	64.41	0.00	<i>43.86</i>	<i>112.84</i>	<i>0.07</i>	<i>0.03</i>	<i>0.00</i>	<i>0.90</i>	<i>0.00</i>	<i>1.00</i>	Siderite rim on early dolomite
19	2.97	1.83	0.17	64.58	0.00	<i>44.33</i>	<i>113.88</i>	<i>0.07</i>	<i>0.03</i>	<i>0.00</i>	<i>0.89</i>	<i>0.00</i>	<i>1.00</i>	Siderite rim on early dolomite
20	2.57	1.34	0.00	62.57	0.00	<i>42.18</i>	<i>108.67</i>	<i>0.07</i>	<i>0.02</i>	<i>0.00</i>	<i>0.91</i>	<i>0.00</i>	<i>1.00</i>	Siderite rim on early dolomite

Note: Analyses 16-20 give very high analytical totals if assumed to be all siderite, based on calculated CO₂. This is due to excess Fe present as finely admixed iron oxide or oxyhydroxide. Calculated ionic ratio (shown in grey italics) assumes that all the iron is present as siderite and does not take account of the admixture with iron oxide.

Sample ST22 G05

Sample ST22 G05 comprises moderately- to poorly sorted fine to medium sandstone, ranging in grain size from silt and very fine sand to coarse sand. In cross section, the tabular cemented sandstone is colour banded with orange-brown bands representing diffuse oxidation fronts impregnated by finely disseminated iron oxyhydroxides. The sand grains are dominantly angular to sub-angular grains (Plate 13). The sand is composed dominantly of detrital quartz, with minor plagioclase, K-feldspar, lithic clasts (including siltstone, chert, and limestone clasts) and calcareous bioclastic detritus (including abraded fragments of mollusc shells and multi-chambered foraminiferal tests), and accessory pyroxene and detrital iron-titanium oxides. It is broadly similar to sample ST21G09, although no glauconite was observed in this sample.

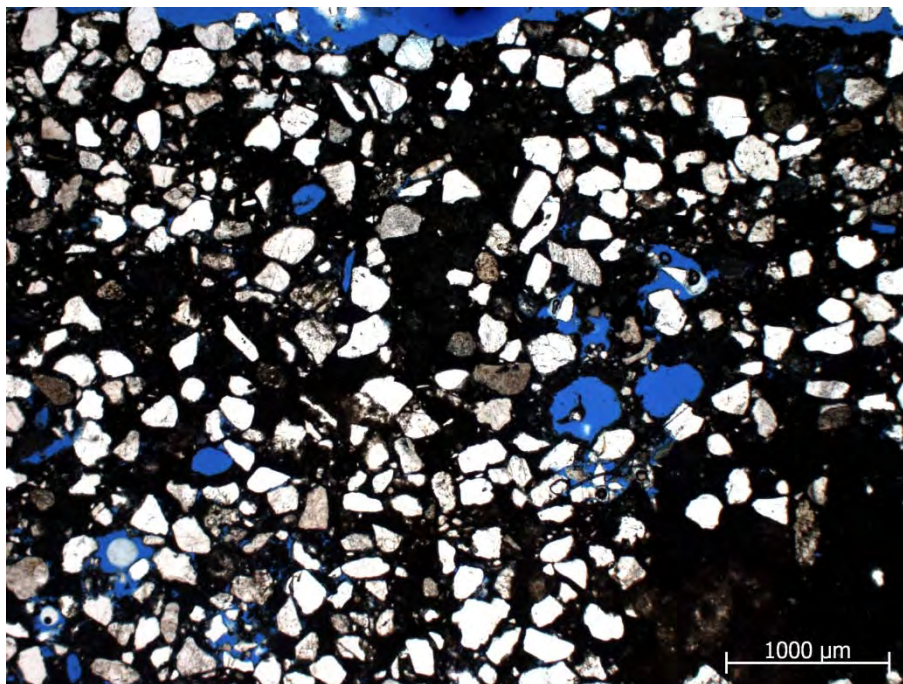


Plate 13. Transmitted light photomicrograph (plane polarised light) of dolomite-cemented fine to medium sandstone, showing angular to sub-angular detrital quartz sand cemented by patchy brown to opaque microdolomite cement. Sample ST22 G05.

The carbonate cement fabrics are also very similar to those described from sample ST21 G09, including:

1. The development of early isopachous fringes of fine-grained dolomite coating grain surface (Plate 14 and Plate 15).
2. Pelloidal grains, spheroidal aggregates or “clots” of micritic or microcrystalline (microsparry) dolomite (Plate 15). As in ST21 G09, these pelloidal grains form the bulk of the carbonate cemented matrix, and their outlines are often delineated by darker staining by iron oxides (*cf.* Plate 14).

Higher magnification observations show that the pelloidal dolomite comprises microbotryoidal or framboidal aggregates of subidiomorphic to idiomorphic rhombic dolomite crystals (Plate 16), often nucleated around a hollow core, and again very similar in morphology to the dolomite observed in ST21 G09. In some cases, cellular structures, partially mineralised by very fine dolomite may be preserved within or on the surface of these framboidal aggregates (Plate 17). The cellular structures are of the order of 1 to 2 µm across and may represent mineralised bacteria.

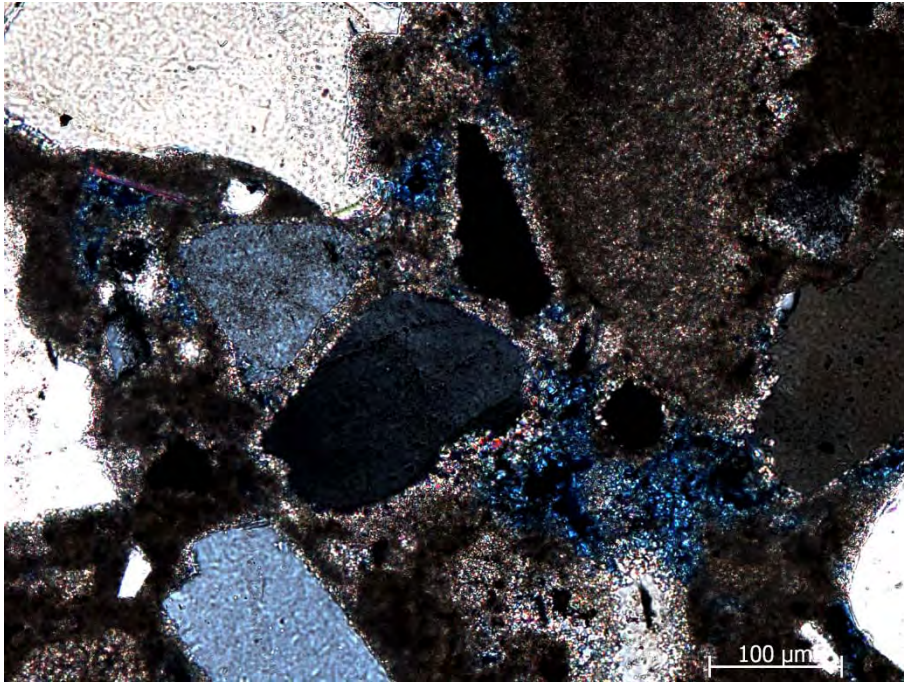


Plate 14. Transmitted light photomicrograph (crossed-polars) showing the development of an early grain-fringing isopachous microdolosparite cement (highly birefringent). Dolomicrite or microsparry dolomite also forms very fine to fine sand-grade “clots” or “pellets”. Sample ST22 G09.

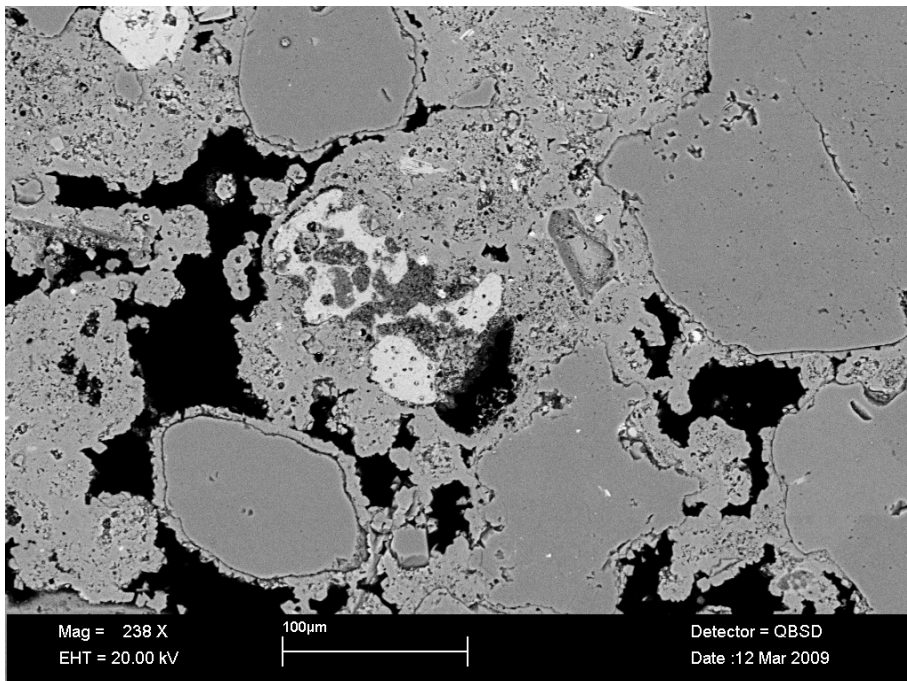


Plate 15. BSEM image showing isopachous microdolospar cement fringes around detrital sand grains, and “clots”, or spheroidal-framboidal aggregates of dolomite microcrystals within the intergranular areas. Sample ST22 G05.

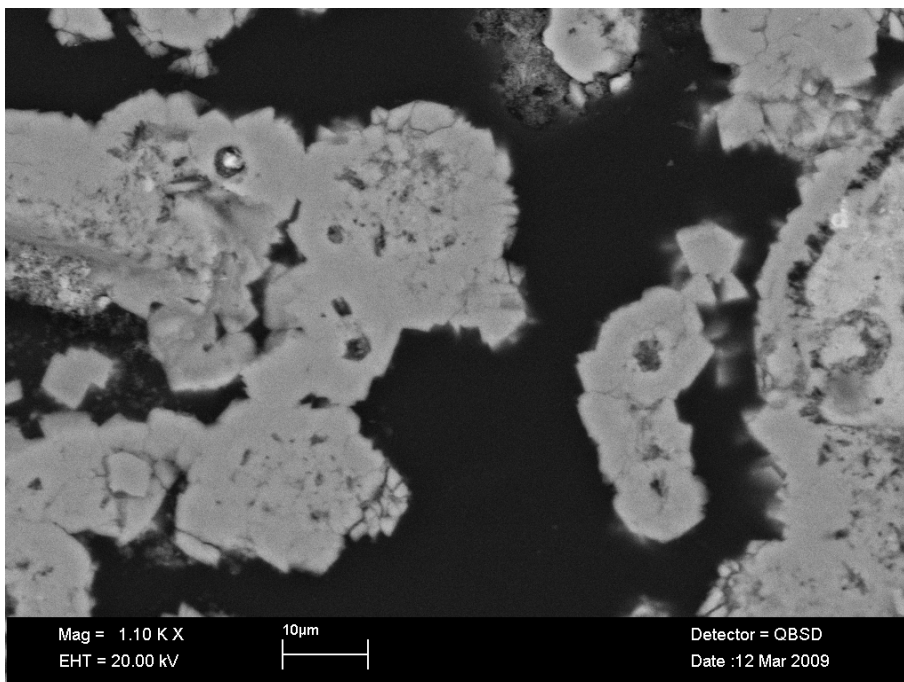


Plate 16. BSEM image showing detail of the microfabric of the microporous dolomite cement. The dolomite consists of “microbotryoidal” or “framboidal” aggregates of rhombic dolomite microcrystals, often nucleated around a “hollow core”. Sample ST22 G05.

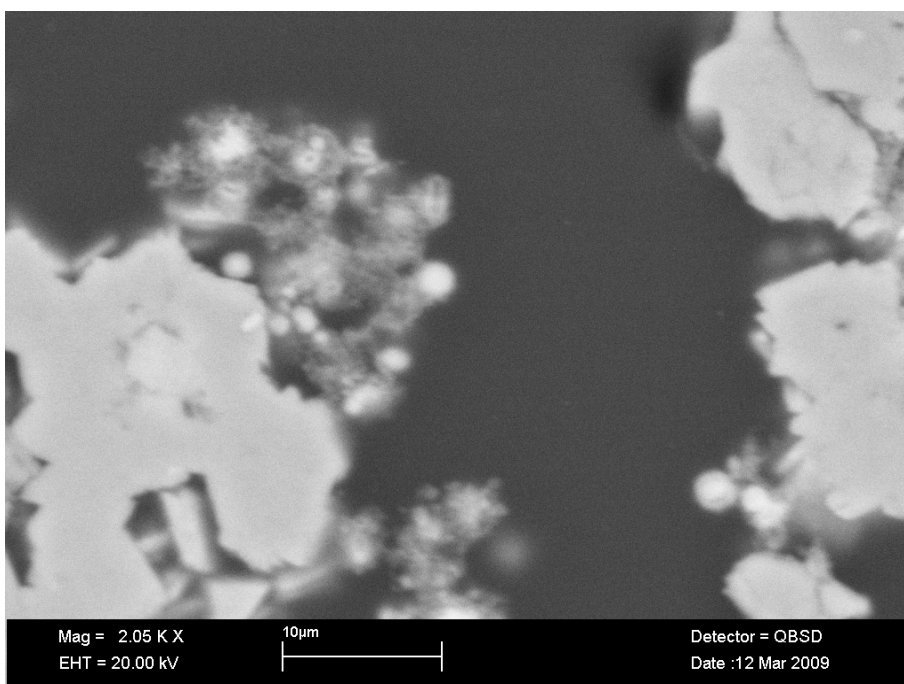


Plate 17. BSEM image showing clusters of very fine cellular structures partially mineralised by dolomite, and associated with framboidal or spherical aggregates of dolomite microcrystals. Sample ST22 G05.

Electron microprobe analyses for the dolomite cements are presented in Table 16 and summarised in Figure 61. As in ST21 G09, the dolomite is characterised by an excess of Ca relative to the ideal stoichiometric composition of dolomite, with up to 10 mole% excess CaCO_3 . Rare rhombs of more calcic carbonate may also be present, although only one quantitative electron microprobe analysis was recorded, which suggested that a small amount of high-magnesium calcite may also be present.

The only significant mineralogical and petrological difference between this sample and sample ST21 G09 is that siderite cement is not present. In all other respects the carbonate cement fabrics of samples ST22 G05 and ST21 G09 are very similar and therefore, they probably have a similar diagenetic origin.

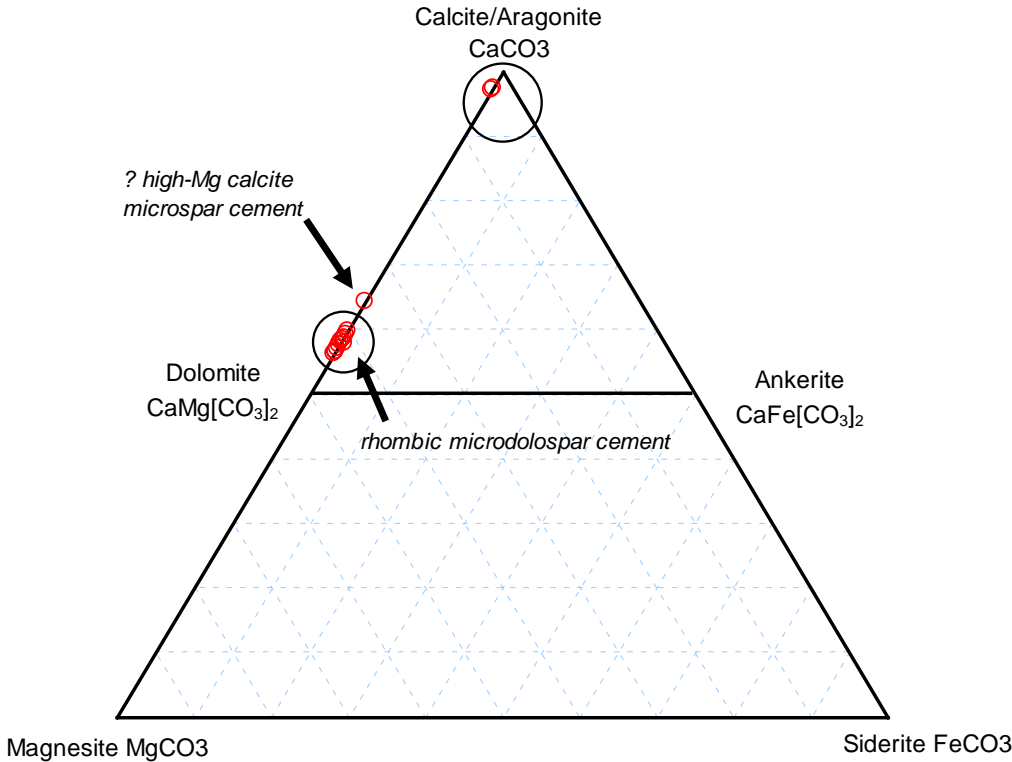


Figure 5. CaCO_3 - MgCO_3 - FeCO_3 molar ratio plot illustrating the composition of the carbonate cements in MDAC sample “ST22 G05”, relative to end-member carbonate minerals

Table 4. Electron microprobe of carbonate cements and other carbonate components in sample ST22 G05

No.	WEIGHT % OXIDE							IONIC RATIO [normalised to 3 [O]						COMMENTS
	MgO	CaO	MnO	FeO	SrO	CO ₂ (calc)	Total wt%	Mg ²⁺	Ca ²⁺	Mn ²⁺	Fe ²⁺	Sr ²⁺	CO ₃ ²⁻	
1	18.64	35.41	0.00	0.00	0.00	48.13	102.18	0.42	0.58	0.00	0.00	0.00	1.00	Fine microsparry dolomite associated with aggregates around a hollow "cell" and forming fringe cement.
2	18.44	34.08	0.00	0.00	0.00	46.87	99.39	0.43	0.57	0.00	0.00	0.00	1.00	Fine microsparry dolomite associated with aggregates around a hollow "cell" and forming fringe cement.
3	17.86	36.16	0.00	0.00	0.00	47.86	101.87	0.41	0.59	0.00	0.00	0.00	1.00	Fine microsparry dolomite associated with aggregates around a hollow "cell" and forming fringe cement.
4	14.92	37.60	0.00	0.00	0.00	45.79	98.31	0.36	0.64	0.00	0.00	0.00	1.00	Fine microsparry high-Mg calcite(?) associated with aggregates around a hollow "cell" and forming fringe cement.
5	18.57	35.95	0.00	0.00	0.00	48.47	102.99	0.42	0.58	0.00	0.00	0.00	1.00	Fine microsparry dolomite associated with aggregates around a hollow "cell" and forming fringe cement.
6	18.26	35.34	0.00	0.39	0.00	47.89	101.88	0.42	0.58	0.00	0.00	0.00	1.00	Rhomb dolomite replacing interstitial clay matrix in tightly cemented band
7	17.39	35.93	0.00	0.00	0.00	47.18	100.50	0.40	0.60	0.00	0.00	0.00	1.00	Rhomb dolomite replacing interstitial clay matrix in tightly cemented band
8	19.32	34.90	0.00	0.00	0.00	48.47	102.68	0.44	0.56	0.00	0.00	0.00	1.00	Rhomb dolomite replacing interstitial clay matrix in tightly cemented band
9	19.30	35.15	0.00	0.00	0.00	48.64	103.09	0.43	0.57	0.00	0.00	0.00	1.00	Rhomb dolomite replacing interstitial clay matrix in tightly cemented band
10	19.63	35.29	0.00	0.00	0.00	49.12	104.04	0.44	0.56	0.00	0.00	0.00	1.00	Pore-filling microdolospar cement
11	18.16	35.83	0.00	0.00	0.00	47.93	101.92	0.41	0.59	0.00	0.00	0.00	1.00	Pore-filling microdolospar cement
12	17.89	34.94	0.00	0.00	0.00	46.94	99.77	0.42	0.58	0.00	0.00	0.00	1.00	Pore-filling microdolospar cement
13	1.09	54.25	0.00	0.00	0.57	44.00	99.91	0.03	0.97	0.00	0.00	0.01	1.00	Detrital limestone clast
14	0.98	54.88	0.00	0.00	0.00	44.12	99.98	0.02	0.98	0.00	0.00	0.00	1.00	Detrital limestone clast

4.4 Sample ST27 G22

Sample ST27 G22 comprises moderately-sorted fine sandstone. In cross section, the tabular cemented sandstone layer displays irregular mottling with orange-brown bands representing diffuse patches of rock that are impregnated by finely disseminated iron oxyhydroxides. The sand grains are dominantly sub-rounded grains (Plate 18). The sand is composed dominantly of detrital quartz, with minor plagioclase, K-feldspar, lithic clasts (including siltstone, chert, altered fine grained silicified or felsic volcanics, and limestone clasts) and calcareous bioclastic detritus, and accessory fresh green glauconite.

The carbonate cement in this sample is more complex than the other samples, and comprises a mixture of predominantly high-magnesium calcite and aragonite. Bulk XRD analysis (Figure 62) also suggests that poorly crystalline dolomite may also be present, although evidence could be found for only minor to trace amounts of dolomite from the petrographical and electron microprobe analyses (Table 17 and Figure 63).

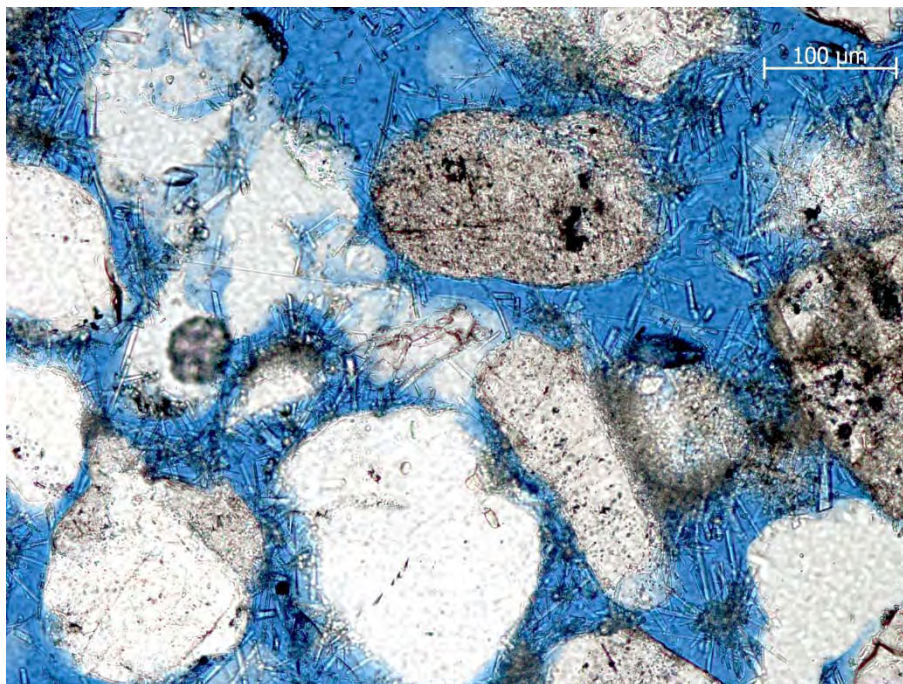


Plate 18. Transmitted light photomicrograph (plane-polarised light) showing porous sand fabric with intergranular pores (blue) lined or partially-filled by fibrous or acicular aragonite crystals, resting on brownish micritic high-magnesium calcite grain-coating fringes. Sample ST27 G22.

The earliest cement fabric observed is the development of a thin isopachous high-magnesium calcite fringe that is sometimes preserved around detrital grains. The bulk of the carbonate cement comprises micritic to microsparry high-magnesium calcite. This typically occurs as “clots” and framboidal or microbotryoidal aggregates of calcite microcrystals (Plate 19 and Plate 20). The calcite may also form meniscus fringes between detrital grains (Plate 18). As in the other samples described above, some of this “clotted micrite” may represent faecal pellets. However, the bulk of the “clots” or micrite aggregates are much finer than the detrital grain size of the sand, and appear to have formed in situ within the intergranular pores. Locally, the micrite may occur as a structureless pore-filling matrix (Plate 21) that may represent areas where these aggregate structures have coalesced. These micritic carbonate fabrics are similar to those described from the other samples and from MDAC elsewhere (see discussions above).

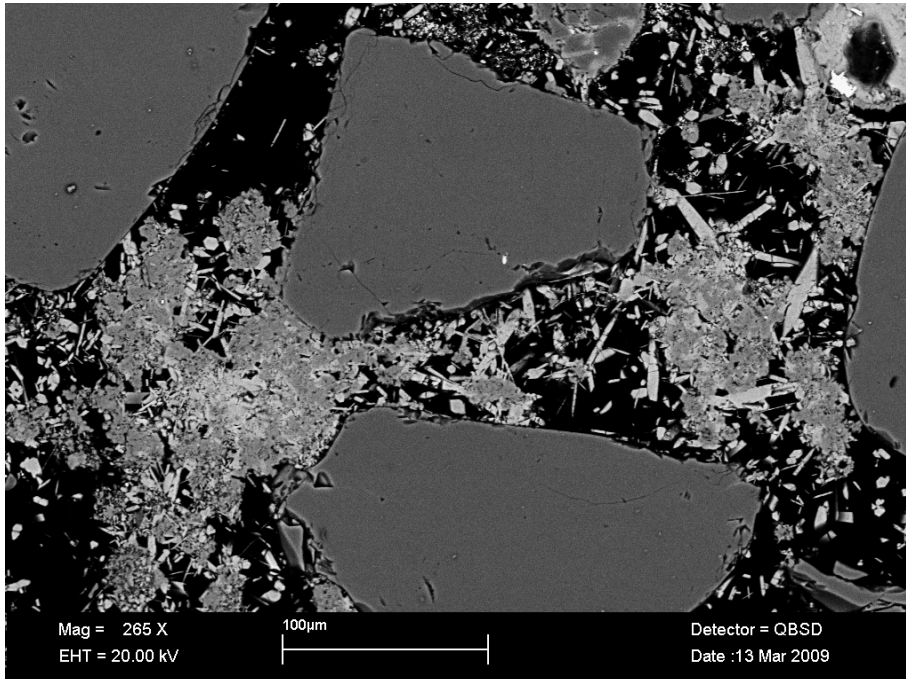


Plate 19. BSEM image showing early spherical clusters or “clots” of microcrystalline (microsparry high-magnesium calcite (mid grey) encrusted by later needles of aragonite. Sample ST27 G22.

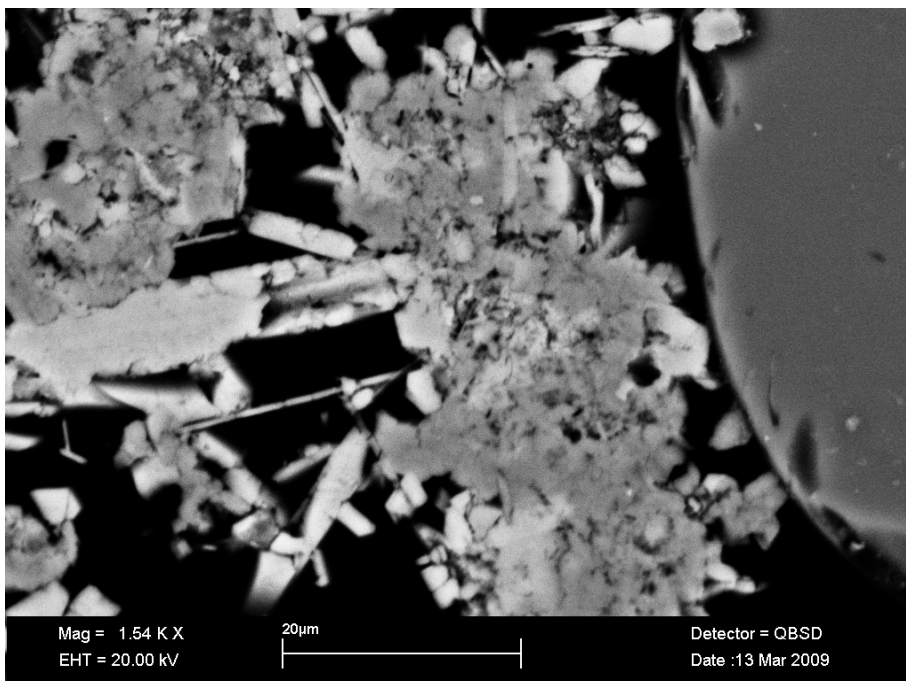


Plate 20. BSEM image showing detail of microcrystalline aggregates of high-magnesium calcite (mid grey) encrusted by later needles of aragonite. Sample ST27 G22.

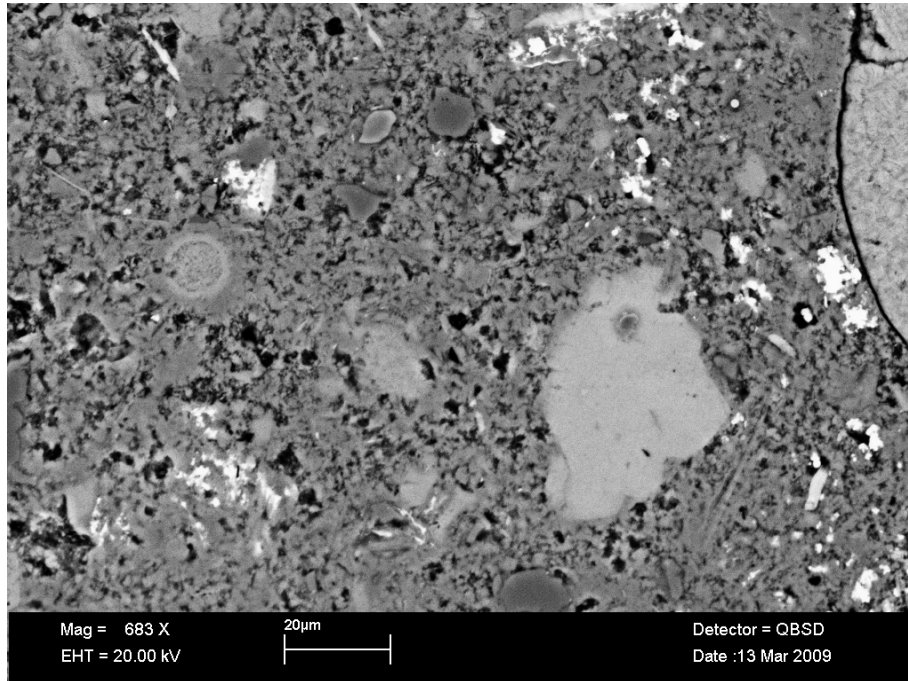


Plate 21. BSEM image of more densely-cemented region of the MDAC sandstone, displaying a matrix cemented by micritic high-magnesium calcite. Fragments of detrital limestone and calcareous microfossils (light grey) can also be seen. ST27 G22.

This sample also contains aragonite (confirmed by XRD analysis - Figure 62). The aragonite is the latest cement fabric formed. It occurs as acicular crystals lining open intergranular pores (Plate 22), resting on and encrusting detrital grains, isopachous high-magnesium calcite fringes and earlier micritic “clots” or aggregates (Plate 19, Plate 20 and Plate 22). Detailed SEM observations show that the aragonite crystals have a well-developed orthorhombic bladed needle-like morphology (Plate 23 and Plate 24). Aragonite needles also form overgrowths on some abraded shell fragments (Plate 25).

Electron microprobe analyses of the carbonate cements from ST27 G22 are presented in Table 17 and are summarised in Figure 63. The data show that the micritic calcite is a very highly magnesium calcite, with between 24 to 38 mole % MgCO_3 in solid-solution. Although this composition is within the range of composition of magnesium calcite recorded in MDAC samples from elsewhere (Jensen *et al.*, 1992) it is much higher than some sites (e.g. Peckmann *et al.*, 2001).

The aragonite cement has a very similar composition to the aragonite in sample ST12 Sledge. It is strontium rich, with up to 1 mole% SrCO_3 in solid-solution.

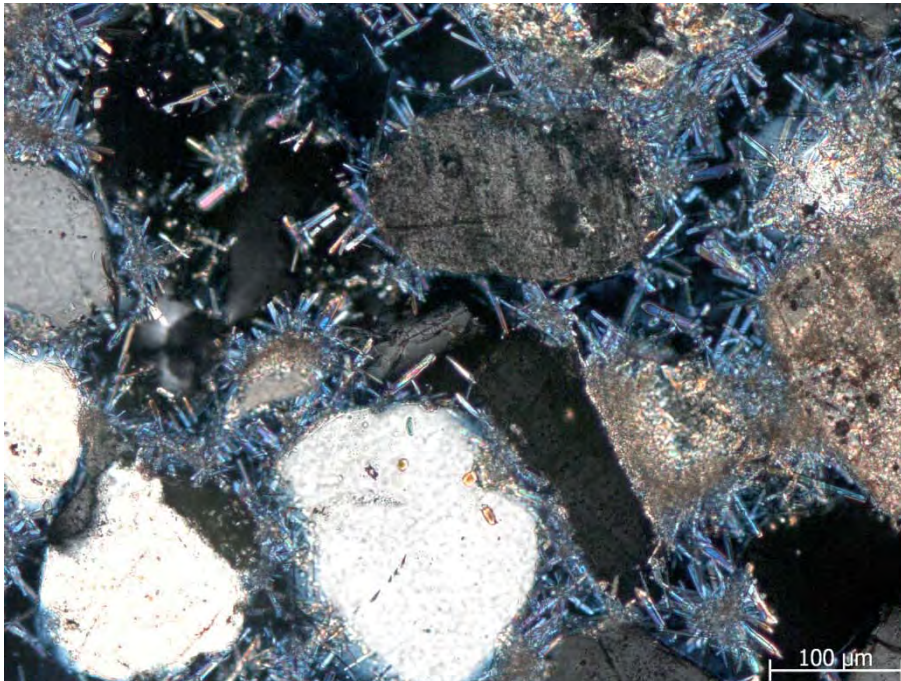


Plate 22. Transmitted light photomicrograph (crossed-polars) of same area as Plate 18, showing highly birefringent acicular aragonite lining intergranular porosity. Sample ST27 G22.

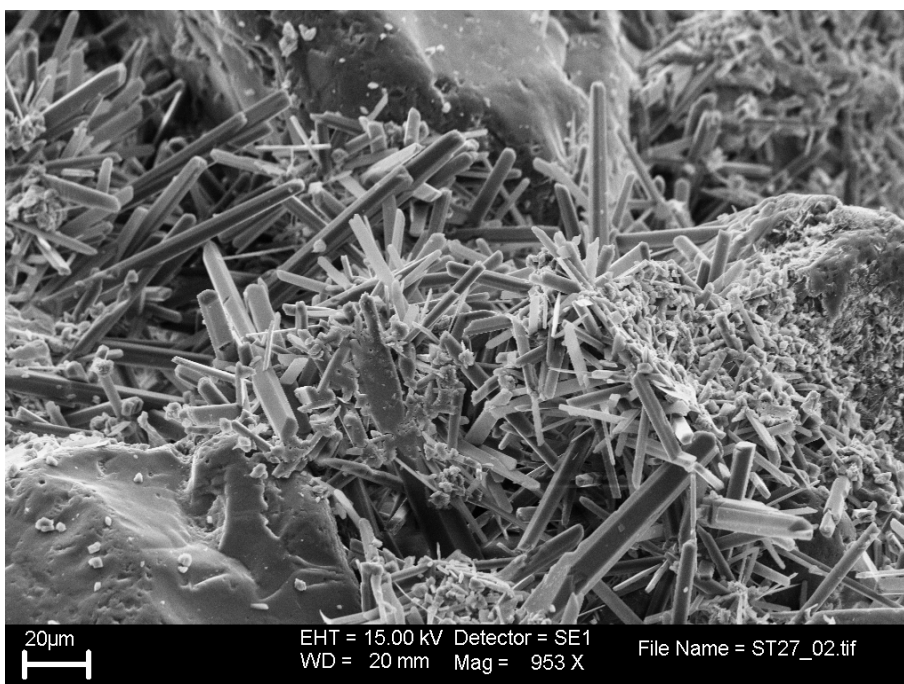


Plate 23. SEM image showing acicular aragonite crystals (needles) nucleated around microporous spherical aggregates of microsparry or micritic high-magnesium calcite. Sample ST27 G22.

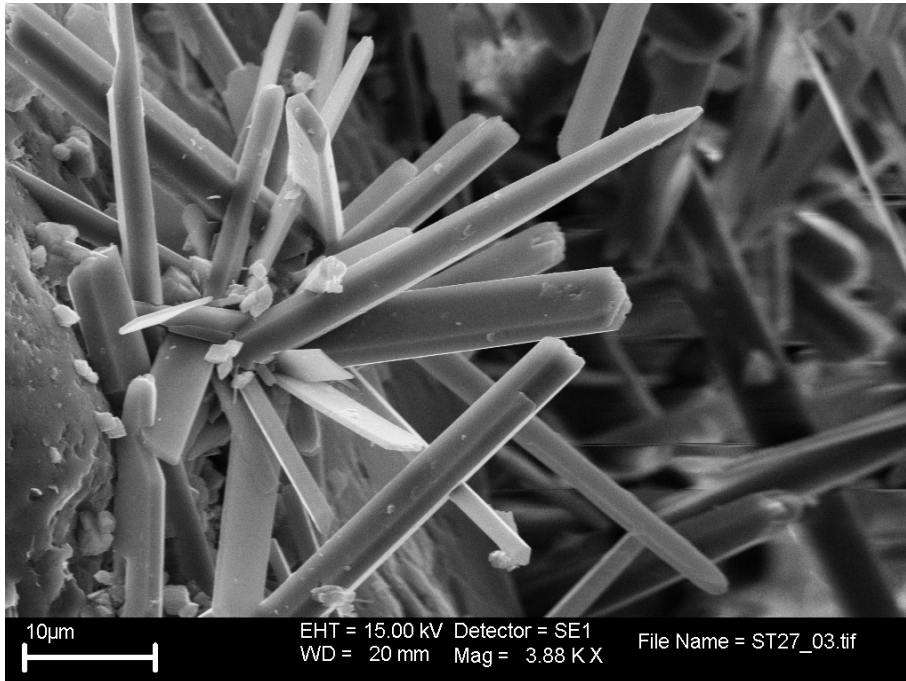


Plate 24. SEM image showing detail of the crystal morphology of the aragonite needles. The crystals display bladed orthorhombic prismatic crystal form. Sample ST27 G22.

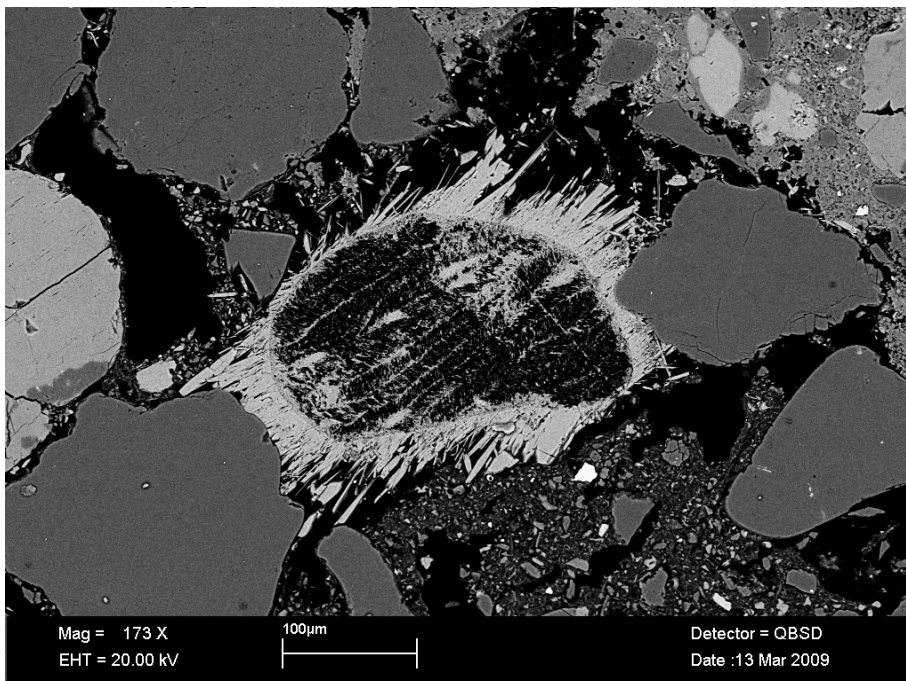


Plate 25. BSEM image showing altered detrital carbonate grain that has dissolved after initially being overgrown by acicular aragonite. ST27 G22.

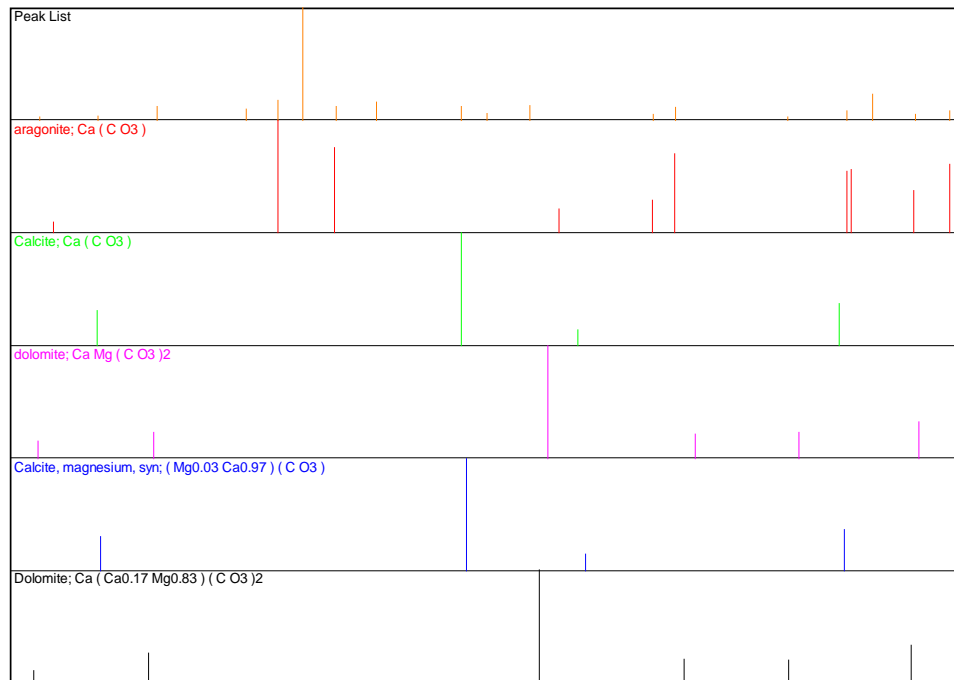
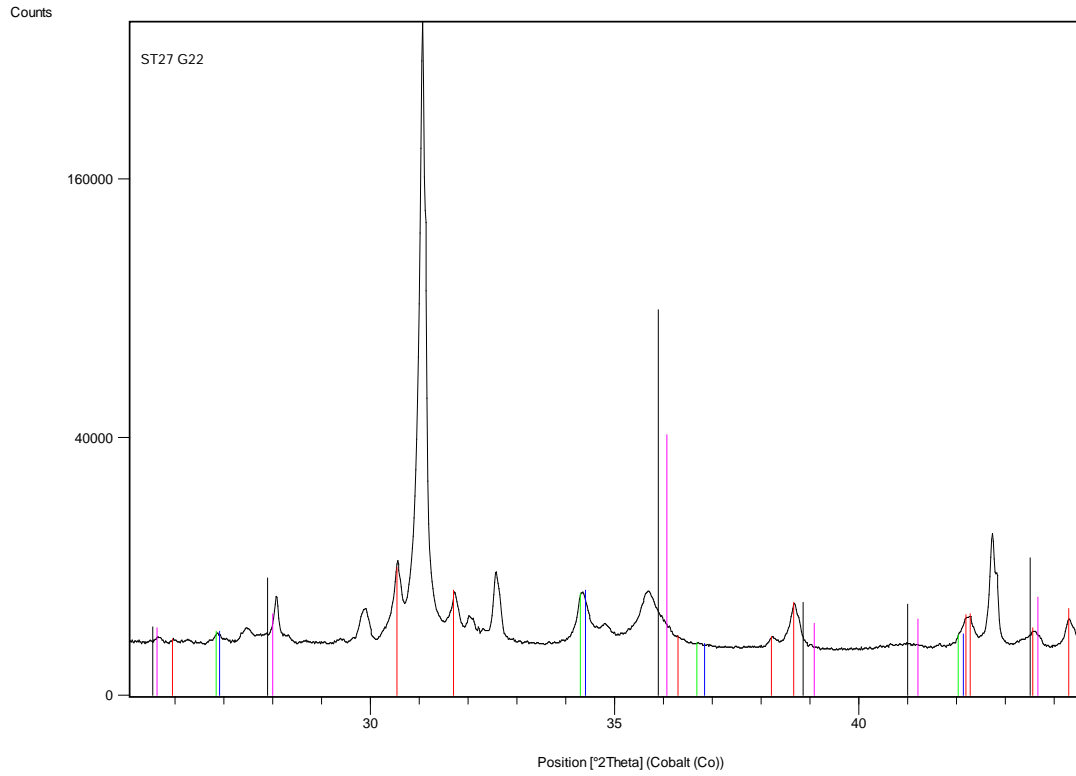


Figure 6. XRD trace for bulk MDAC sample ST27 G22 and comparison with reference patterns (“stick patterns”) for potential carbonate minerals

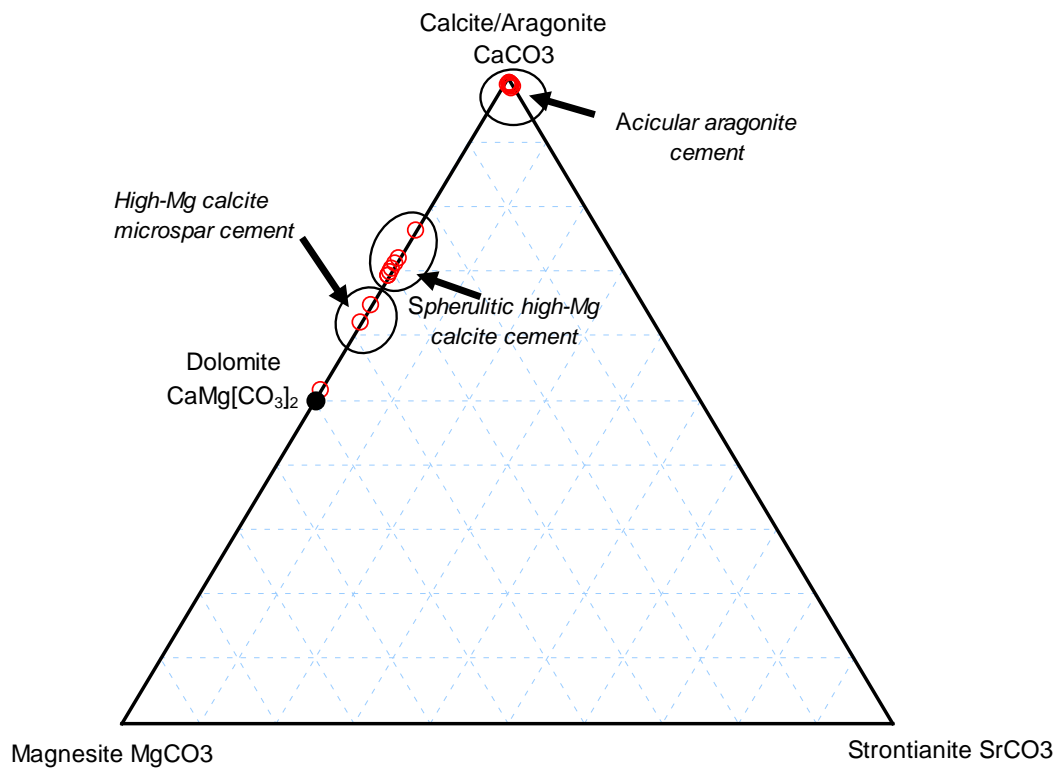


Figure 7. CaCO_3 - MgCO_3 - SrCO_3 molar ratio plot illustrating the composition of the carbonate cements in MDAC sample “ST27 G22”, relative to end-member carbonate minerals

Table 5. Electron microprobe of carbonate cements and other carbonate components in sample ST27 G22

No.	WEIGHT % OXIDE							IONIC RATIO [normalised to 3 [O]						COMMENTS
	MgO	CaO	MnO	FeO	SrO	CO ₂ (calc)	Total wt%	Mg ²⁺	Ca ²⁺	Mn ²⁺	Fe ²⁺	Sr ²⁺	CO ₃ ²⁻	
1	0.00	54.11	0.00	0.00	0.89	42.83	97.82	0.00	0.99	0.00	0.00	0.01	1.00	Acicular aragonite growing in open intergranular porosity
2	0.00	55.10	0.00	0.00	1.11	43.70	99.92	0.00	0.99	0.00	0.00	0.01	1.00	Acicular aragonite growing in open intergranular porosity
3	0.17	56.39	0.00	0.00	0.79	44.76	102.10	0.00	0.99	0.00	0.00	0.01	1.00	Acicular aragonite growing in open intergranular porosity
4	0.00	54.21	0.00	0.00	1.06	42.98	98.25	0.00	0.99	0.00	0.00	0.01	1.00	Acicular aragonite growing in open intergranular porosity
5	0.20	55.77	0.00	0.00	0.98	44.39	101.35	0.00	0.99	0.00	0.00	0.01	1.00	Acicular aragonite growing in open intergranular porosity
6	0.00	53.31	0.00	0.00	1.15	42.31	96.77	0.00	0.99	0.00	0.00	0.01	1.00	Acicular aragonite growing in open intergranular porosity
7	0.00	56.19	0.00	0.00	1.19	44.60	101.98	0.00	0.99	0.00	0.00	0.01	1.00	Acicular aragonite growing in open intergranular porosity
8	0.00	55.32	0.00	0.00	0.86	43.77	99.96	0.00	0.99	0.00	0.00	0.01	1.00	Acicular aragonite growing in open intergranular porosity
9	0.00	55.39	0.00	0.00	1.29	44.01	100.69	0.00	0.99	0.00	0.00	0.01	1.00	Acicular aragonite overgrowths on bioclastic debris
10	0.00	55.81	0.00	0.00	1.56	44.45	101.83	0.00	0.99	0.00	0.00	0.01	1.00	Acicular aragonite overgrowths on bioclastic debris
11	0.00	55.72	0.00	0.00	0.85	44.08	100.64	0.00	0.99	0.00	0.00	0.01	1.00	Acicular aragonite overgrowths on bioclastic debris
12	0.18	55.18	0.00	0.00	1.42	44.10	100.89	0.00	0.98	0.00	0.00	0.01	1.00	Acicular aragonite overgrowths on bioclastic debris
13	0.00	55.38	0.00	0.00	1.27	43.99	100.63	0.00	0.99	0.00	0.00	0.01	1.00	Acicular aragonite overgrowths on bioclastic debris
14	12.39	38.70	0.00	0.00	0.00	43.89	94.97	0.31	0.69	0.00	0.00	0.00	1.00	Microporous high-Mg calcite microsparite spherulite "cores" surrounded by later acicular aragonite

No.	WEIGHT % OXIDE							IONIC RATIO [normalised to 3 [O]]						COMMENTS
	MgO	CaO	MnO	FeO	SrO	CO ₂ (calc)	Total wt%	Mg ²⁺	Ca ²⁺	Mn ²⁺	Fe ²⁺	Sr ²⁺	CO ₃ ²⁻	
15	11.64	41.36	0.00	0.00	0.00	45.16	98.16	0.28	0.72	0.00	0.00	0.00	1.00	Microporous high-Mg calcite microsparite spherulite "cores" surrounded by later acicular aragonite
16	9.27	41.46	0.00	0.00	0.00	42.65	93.37	0.24	0.76	0.00	0.00	0.00	1.00	Microporous high-Mg calcite microsparite spherulite "cores" surrounded by later acicular aragonite
17	12.64	39.67	0.00	0.00	0.00	44.91	97.22	0.31	0.69	0.00	0.00	0.00	1.00	Microporous high-Mg calcite microsparite spherulite "cores" surrounded by later acicular aragonite
18	12.02	38.69	0.00	0.00	0.00	43.48	94.19	0.30	0.70	0.00	0.00	0.00	1.00	Microporous high-Mg calcite microsparite spherulite "cores" surrounded by later acicular aragonite
19	11.26	38.48	0.00	0.00	0.00	42.48	92.22	0.29	0.71	0.00	0.00	0.00	1.00	Microporous high-Mg calcite microsparite spherulite "cores" surrounded by later acicular aragonite
20	11.96	39.36	0.00	0.00	0.00	43.93	95.25	0.30	0.70	0.00	0.00	0.00	1.00	Microporous high-Mg calcite microsparite spherulite "cores" surrounded by later acicular aragonite
21	14.63	37.44	0.19	0.69	0.00	45.89	98.84	0.35	0.64	0.00	0.01	0.00	1.00	High-Mg calcite cement forming major cement in tightly cemented area
22	20.56	30.53	0.70	0.48	0.00	47.12	99.39	0.48	0.51	0.01	0.01	0.00	1.00	Dolomite crystals within cement forming major cement in tightly cemented area
23	15.37	34.73	0.00	0.89	0.00	44.57	95.56	0.38	0.61	0.00	0.01	0.00	1.00	High-Mg calcite cement forming major cement in tightly cemented area

Note: Low analytical totals are due to microporous nature of the fine grained cements.

4.5 Sample ST35 G17

Sample ST35 G17 comprises well-cemented fine sandstone. The sand is composed dominantly of detrital quartz, with minor plagioclase, K-feldspar, lithic clasts (including siltstone, chert, altered fine grained silicified or felsic volcanics, and limestone clasts) and calcareous bioclastic detritus, and accessory fresh green glauconite. The rock has an extensive micritic carbonate matrix with patches of more open intergranular porosity. An early generation of high-magnesium calcite forms well-developed isopachous fringes around many of the detrital grains (Plate 26). These are often seen to be surrounded by a halo of fine iron oxyhydroxide staining, which may enclose relicts of oxidised framboidal pyrite (Plate 26). The presence of framboidal pyrite in close association with the carbonate cements indicates that bacterial sulphate reduction is also occurring during carbonate precipitation. The micritic matrix is composed fine grained high-magnesium calcite. In more densely-cemented areas the micrite matrix appears structureless but more porous regions of the sample display “clotted”, framboidal or microbotryoidal aggregate micrite fabrics (Plate 27) similar to those described from sample ST27 G22

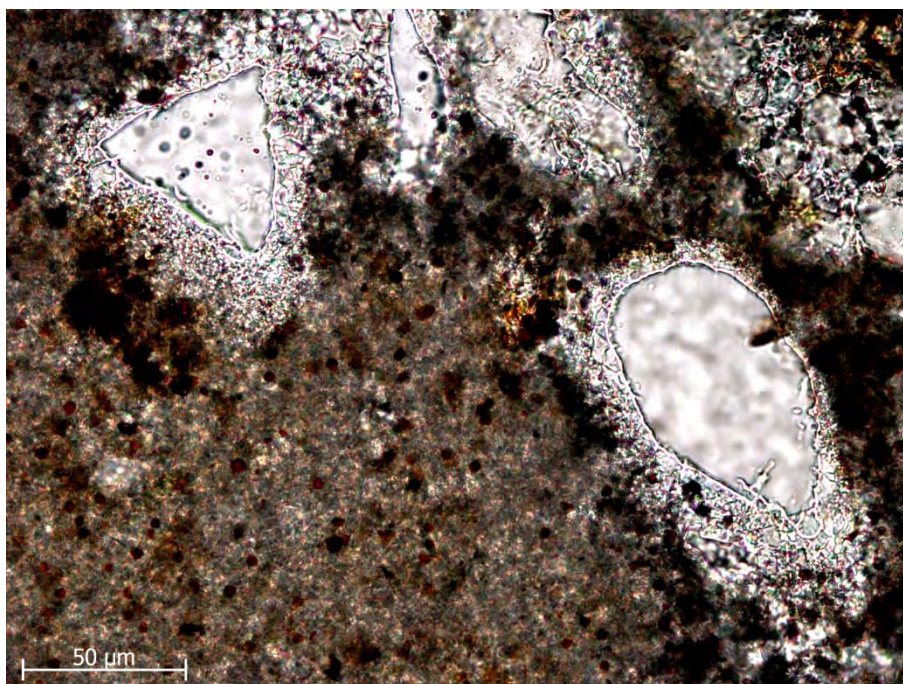


Plate 26. Transmitted light photomicrograph (plane-polarised light) showing early microcrystalline fringe of high-magnesium calcite cement around detrital quartz grains, enclosed within a fine dense micritic high-magnesium calcite matrix. Framboidal brown to opaque iron oxide or iron oxyhydroxide (after oxidised pyrite) is concentrated on the surface of the earlier calcite fringe cement, and is also less abundantly, disseminated through the later micritic calcite matrix. Sample ST35 G17.

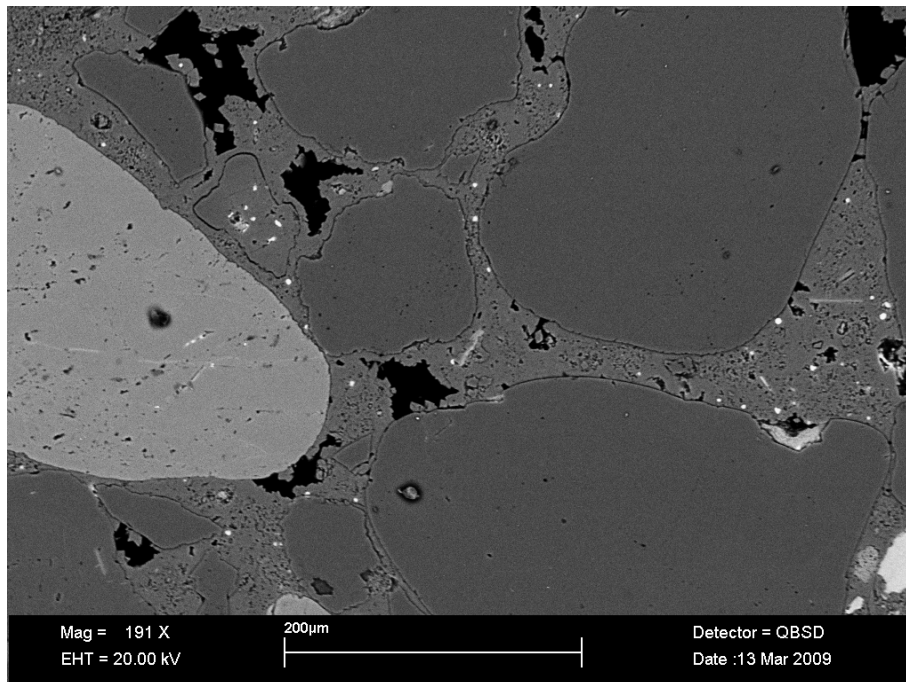


Plate 27. BSEM image showing grain-coating fringes of microcrystalline high-magnesium calcite, and areas of intergranular porosity filled by denser microcrystalline high-magnesium calcite cement. Bright grains of iron oxyhydroxide can be seen close to the grain margins. Sample ST35 G17.

4.6 Sample ST36 RD04

Sample ST36 RD04 comprises a medium to fine sandstone, containing predominantly angular to sub-angular detrital grains and a minor proportion of well-rounded (?aeolian-derived) sand (Plate 28). The sand is composed dominantly of detrital quartz, with minor plagioclase, K-feldspar, lithic clasts (including siltstone, chert, altered fine grained silicified or felsic volcanics, and limestone clasts) and calcareous bioclastic detritus, and fresh green glauconite is a common accessory component

The matrix of the rock comprises largely carbonate-cemented siliciclastic clay and silt. Bulk XRD analysis indicates that the carbonate is predominantly calcite, with XRD peak shift and peak broadening suggesting that it is probably largely high-magnesium calcite with minor poorly-ordered dolomite (Figure 64). The magnesium-rich composition of the calcite was confirmed by BSEM-EDXA. The carbonate matrix is often heavily iron-stained and sometimes almost opaque in thin section. The iron staining often delineates a well-developed pelloidal fabric (Plate 29). In contrast to the other samples described above, the majority of these pelloidal grains have a grain size similar to that of the detrital quartz sand and appear to form part of the sandstone's generally grain-supported fabric (Plate 29 and Plate 30). Detailed BSEM-EDXA observations (Plate 30) show that these pelloids consist of a very intimate admixture of very fine grained high-magnesium calcite and siliciclastic silt and clay. These observations suggest that the bulk of these pelloidal grains are probably faecal pellets composed of biologically-reworked micrite and detrital silt and clay sediment.

Only a very minor amount of the carbonate cement appears to be of in situ origin in this sample. Primary high-magnesium calcite is present as a very minor component, occasionally present as fine equant idiomorphic crystals forming a grain coating on some detrital silicate grains (Plate 31).

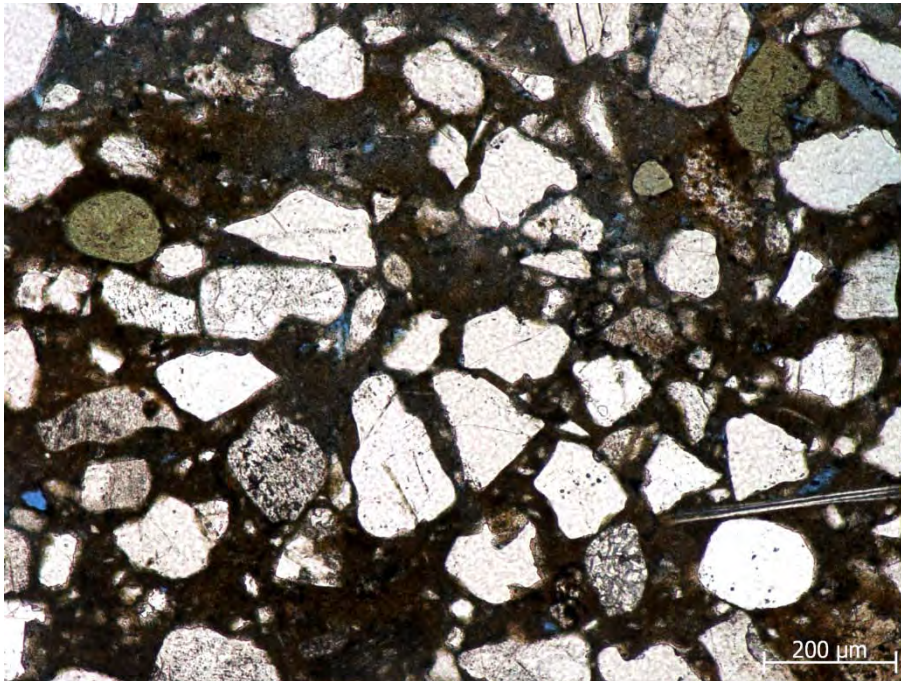


Plate 28. Transmitted light photomicrograph (plane-polarised light) showing angular and subangular grains of detrital quartz (clear), feldspar (cloudy), glauconite (green) and shell fragments, cemented by a brownish micritic matrix of high-magnesium calcite. Sample ST36 RD04.

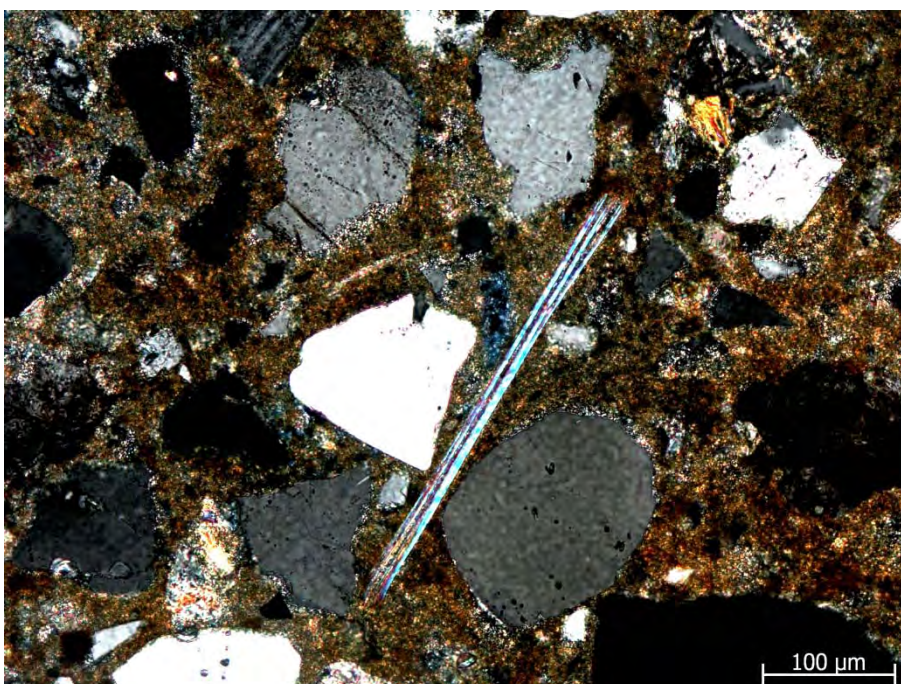


Plate 29. Transmitted light photomicrograph (crossed polars) showing brownish birefringence of iron-stained micritic high-magnesium calcite forming intergranular matrix cement. Traces of early isopachous grain-fringing high-magnesium cement can be seen around some detrital grains. The micritic calcite cement displays a pelloidal fabric. Sample ST36 RD04.

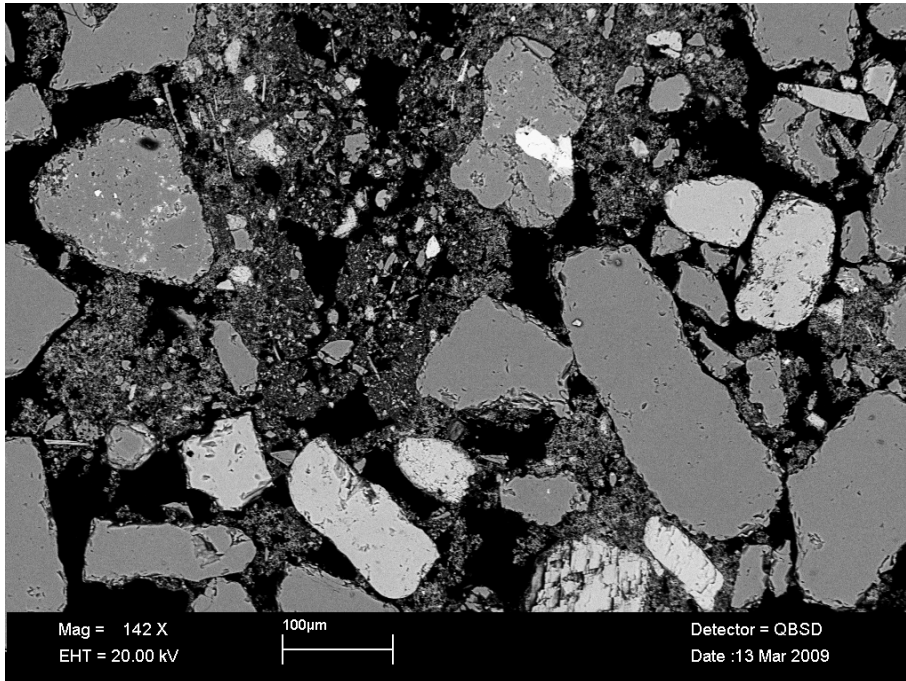


Plate 30. BSEM image showing angular detrital quartz sand with sand-grade pellets of silt and clay cemented by micritic high-magnesium calcite. Sample ST36 RD04

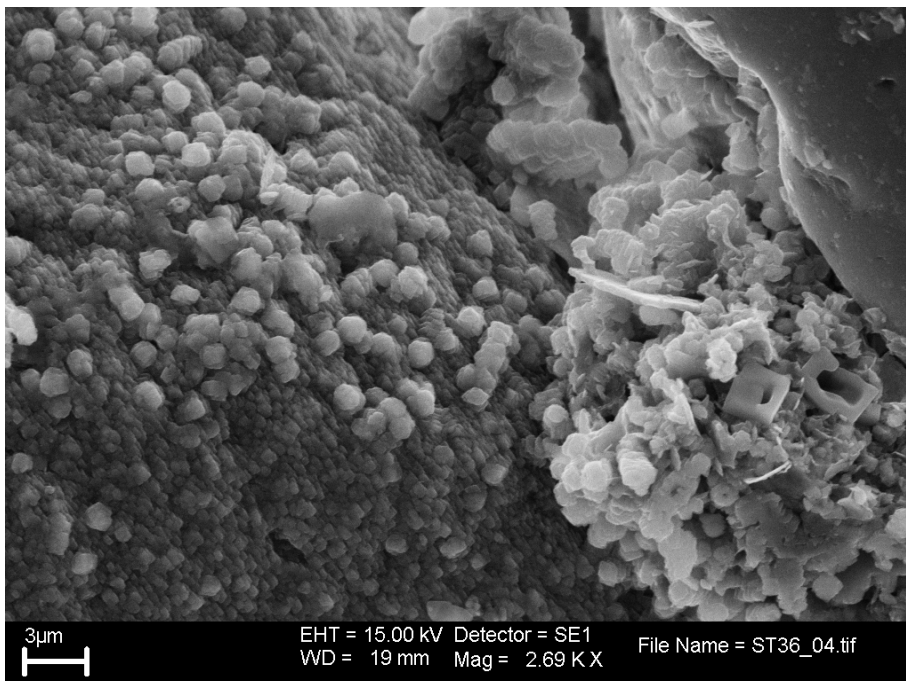


Plate 31. SEM image showing fine equant to rhombohedral crystallites of high-magnesium calcite forming an early grain coating fringe cement. Sample ST36 RD04.

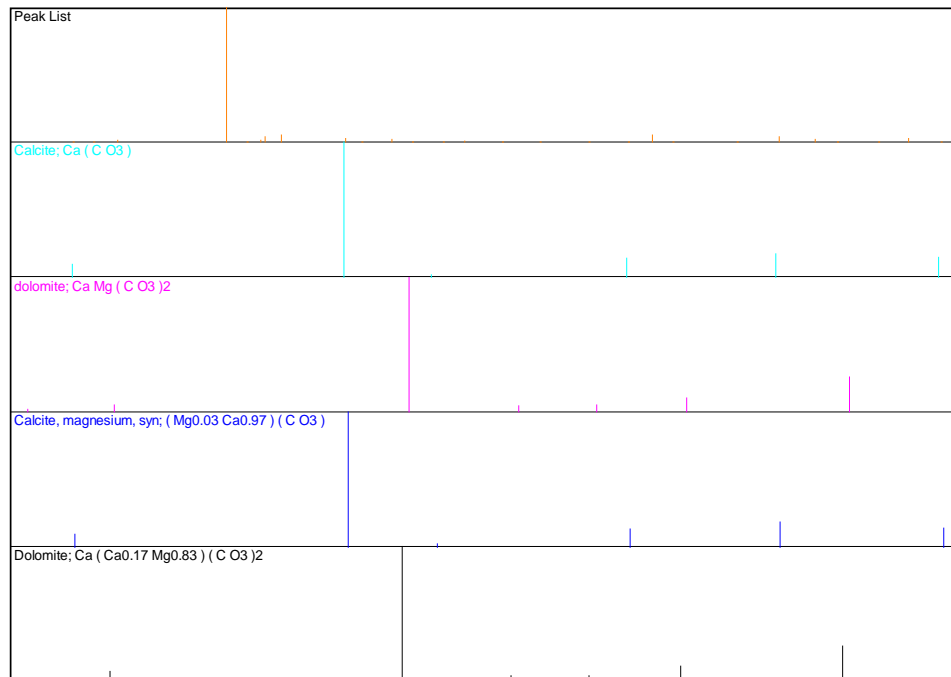
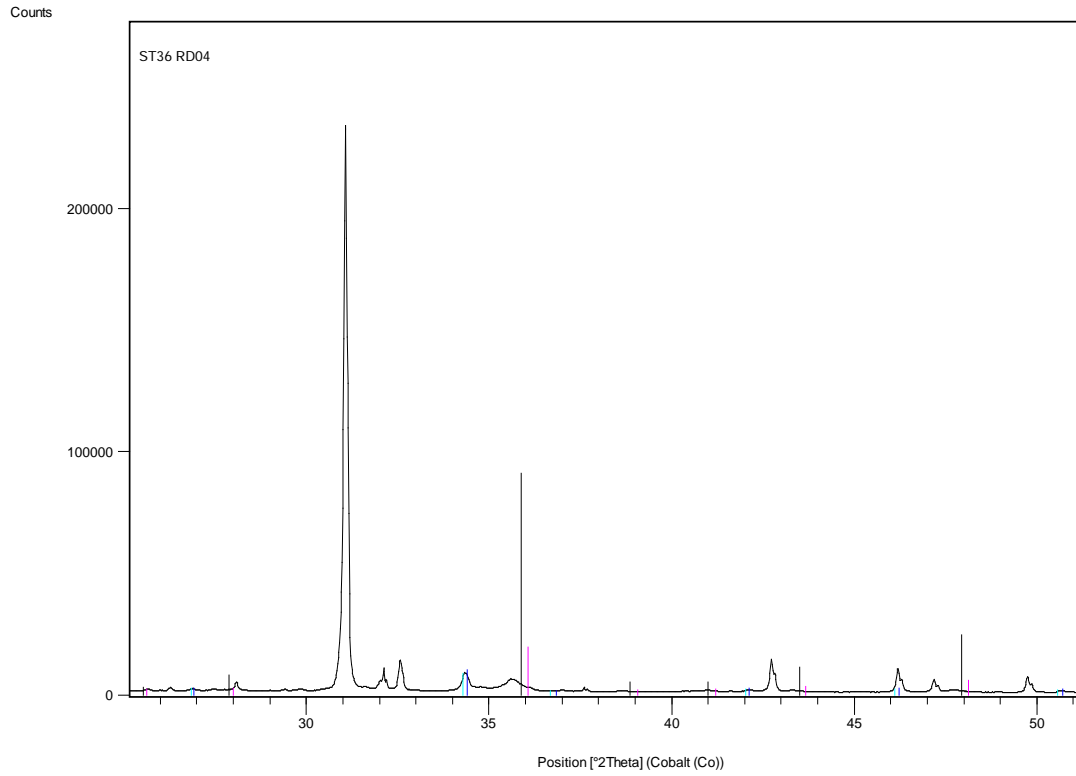


Figure 8. XRD trace for bulk MDAC sample ST36 RD04 and comparison with reference patterns (“stick patterns”) for potential carbonate minerals

Stable isotope characteristics

5.1 General

The results of the stable isotope ($\delta^{13}\text{C}$ and $\delta^{18}\text{O}$) analysis of bulk and microsampled carbonate material from the MDAC samples are given in Table 18. The data include results for the isotopic composition of the bulk carbonate for each sample and data for discrete parts of each sample that were microsampled to try to extract discrete carbonate components or specific generations of carbonate cement. All six bulk samples were successfully analysed. Ten of the microdrilled subsamples failed because they contained insufficient carbonate for analysis. These subsamples attempted to extract the very thin isopachous grain-coating carbonate cements from largely open and very porous parts of the MDAC samples. The amount of carbonate mineral likely to have been recovered in these microsamples was very small and it seems that the microdrilling most probably sampled either mainly the epoxy-resin filling the intergranular porosity in the polished blocks and/or largely non-carbonate parent detrital grains.

The variation in the $\delta^{13}\text{C}$ and $\delta^{18}\text{O}$ characteristics of the MDAC carbonates is summarised in Figure 65.

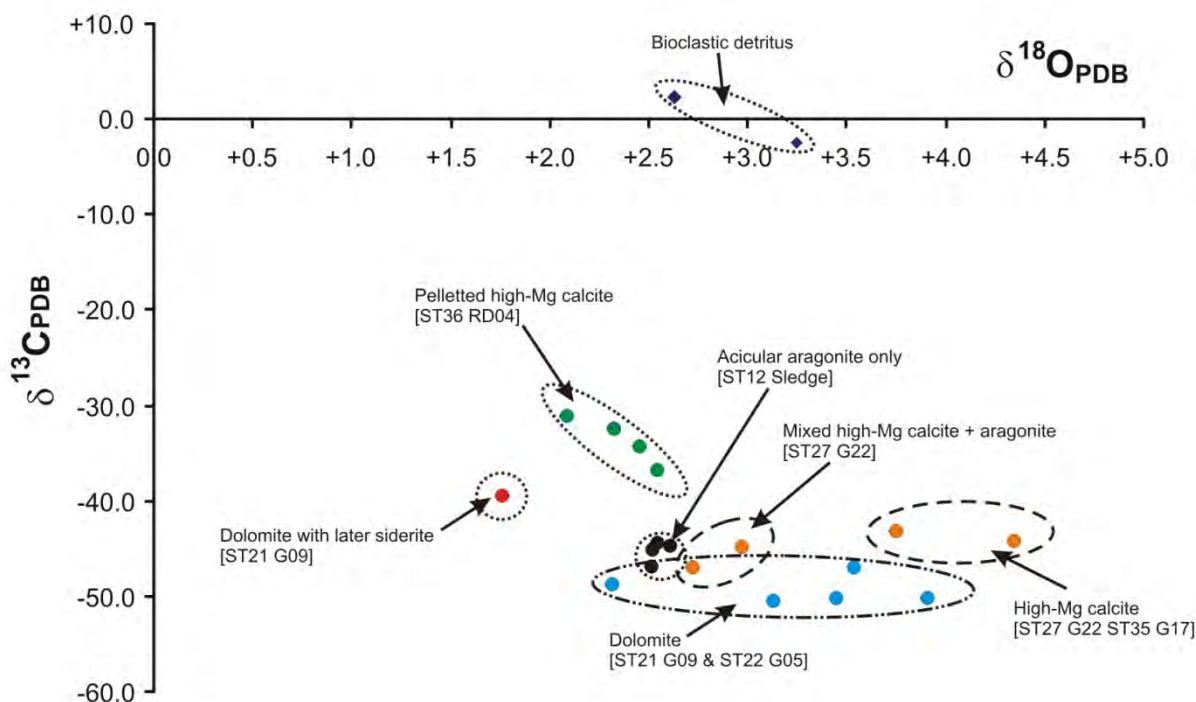


Figure 9. Cross-plot of $\delta^{13}\text{C}$ and $\delta^{18}\text{O}$ illustrating the variation in stable isotopic composition for the MDAC samples

5.2 Carbon isotope composition

The carbon isotopic composition of diagenetic cements varies significantly depending on the process producing the carbonate/bicarbonate ions in the porewater from the breakdown of organic matter. Negative $\delta^{13}\text{C}$ values, typically between 0 to 20 = 0‰ (relative to PDB), are generated by the bacterial reduction of iron, manganese and sulphate (Claypool and Kaplan, 1974; Coleman, 1985; Mozley and Burns, 1993). More positive $\delta^{13}\text{C}$ values, are produced during methanogenesis with deeper burial below the zone of bacterial reduction (Claypool and Kaplan, 1974; Coleman, 1985; Mozley and Burns, 1993). Carbonates with $\delta^{13}\text{C}$ values lighter than -25‰

(relative to PDB) are characteristic of sediments where methane oxidation has produced CO₂ depleted in ¹³C (Pirrie and Marshall, 1991; Mozley and Burns, 1993).

With the exception of two of the subsamples representing bioclastic (mollusc shell) fragments that were analysed from samples ST12 Sledge and ST35 G17, all of the MDAC carbonate analyses display highly depleted ¹³C composition., with δ¹³C_{PDB} values between -31 to -51‰ (Figure 65). These values are strongly indicate of carbonate precipitated as a result of methane oxidation, and are characteristic of MDAC deposits described previously from other areas (Jensen *et al.*, 1992; Sakai *et al.*, 1992; Bohrmann *et al.*, 1998; Peckmann *et al.*, 2001; Muralidhar *et al.*, 2006; Forsberg *et al.*, 2007). The carbon isotope data (Table 18 and Figure 65) therefore lend strong support to the hypothesis that the carbonate-cemented sandstones analysed here from the Mid Irish Sea also represent MDAC.

5.3 Oxygen isotope composition

The temperature at which the carbonate cement precipitated can be estimated from the temperature-dependant equilibrium oxygen isotope fractionation (δ¹⁸O) between the carbonate mineral and the water from which it has precipitated, assuming the carbonate is in equilibrium with the water. The calcite-water system is the best understood carbonate mineral system and is most widely used in palaeotemperature studies, and there are a number of published empirical palaeotemperature equations for the equilibrium precipitation of calcite from solution (Leng and Marshall, 2004). Two such equations were used in this study, to estimate the temperature for the formation of the MDAC in the Mid Irish Sea:

Equation 1: Hays and Grossman's (1991) equation based on their revised 'fit' of O'Neil *et al.*'s (1969) experimental data. This gives very similar results to most other equations.

$$T = 15.7 - 4.36(c-w) + 0.12(c-w)^2$$

Equation 2: Leng and Marshall's (2004) expression of Kim and O'Neil's (1997) more recent equation. This gives slightly lower calculated palaeotemperatures than Equation 1 and other published equations.

$$T = 13.8 - 4.58(c-w) + 0.08(c-w)^2$$

In both cases, T is the temperature (°C), c is δ¹⁸O of calcite relative to the Pee Dee Belemnite (PDB) international standard, and w is the δ¹⁸O of the water relative to the Standard Mean Ocean Water (SMOW) international standard. The calculations made in this report have assumed the oxygen isotope composition of the seawater on the bed of the Mid Irish Sea to be the same as SMOW (i.e. δ¹⁸O = 0‰).

These equations are based on the empirical relationship between temperature, the isotopic composition of calcite, and the composition of the water from which it formed. Aragonite and magnesium calcites precipitated at equilibrium are generally isotopically heavier than pure or low-magnesium calcites. Review of published literature indicates that aragonite δ¹⁸O values are typically around +0.6‰ higher than the equivalent calcite (Leng and Marshall, 2004). The δ¹⁸O values of magnesium calcites typically increase by 0.06‰ per mol% of MgCO₃ in solid-solution in the calcite (Tarutani *et al.*, 1969, cited in Leng and Marshall, 2004). These offsets in δ¹⁸O appear to be independent of temperature (*cf.* Kim and O'Neil, 1997). Dolomite similarly tends to be isotopically heavier than calcite precipitated under the same environment. Land (1980), also cited by Leng and Marshall (2004), indicates that δ¹⁸O values for dolomite are generally around +3‰ heavier than the equivalent calcite mineralisation, at normal surface temperatures.

The isotopic composition of carbonates that should precipitate in equilibrium with the seawater, at present-day seabed temperatures in the Mid Irish Sea area, was also calculated using quadratic

solution of Equation 1, for comparison to the MDAC carbonates (taking into account the offset in $\delta^{18}\text{O}$ values between that for pure calcite and for aragonite, high-magnesium calcite and dolomite, discussed above). For these calculations, the present-day seabed temperature within the area of study was estimated to be between 10.5 and 11°C based on published maps from the JNCC Irish Sea Pilot Study (JNCC, 2003).

Based on these calculations, the $\delta^{18}\text{O}$ of the aragonite from sample ST12 Sledge, and high-magnesium calcite MDAC cements from samples ST27 G22 and ST35 G17 (Table 18 and Figure 65) appear to be slightly heavier than the composition of carbonate predicted to be in equilibrium with seawater under present-day Mid Irish Sea sea-bed temperatures (1.7 to 1.8‰_{PDB} for aragonite; and 2.5 to 3.5‰_{PDB} for high magnesium calcite). These data suggest that these MDAC cements may have precipitated under colder conditions than present-day (calculations suggest between 3 to 6°C for the aragonite, and between 1 to 10°C for the high-magnesium calcite, depending on which equation (above) is used. The carbonate cements in these samples occur as pore-lining or pore filling cements.

In contrast, the high-magnesium calcite in sample ST36 RD04 (Table 18 and Figure 65) appears to have a slightly heavier $\delta^{18}\text{O}$ value than high-magnesium calcite of similar chemistry predicted to form at equilibrium under present-day temperatures. Calculated palaeotemperatures for this sample (assuming equilibrium) are between 0 to 6°C warmer than present seabed temperature. This MDAC sample is markedly different to the other samples, in that it is dominated by cemented pellets composed of micritic high magnesium calcite, rather than occurring as a microsparry pore-filling or isopachous grain-coating intergranular cement that characterises the other samples. The pelloidal fabric of this MDAC sample indicates that the carbonate precipitate has been affected by biological reworking, probably by feeding benthic biota, and may have been modified either by partial recrystallisation in the animal gut and/or subsequent diagenetic processes affecting the sediment. The $\delta^{18}\text{O}$ value of the dolomite cements in samples ST21 G09 and ST22 G05 (Table 18 and Figure 65) are similarly about 0 to 2‰ lighter than dolomite expected to be in equilibrium with present day sea-bed conditions, and again may indicate that it may have formed under slightly warmer conditions. However, the data are very limited and show a relatively wide variation, and the analysed samples may be complicated by the presence of more than one generation of carbonate mineral (e.g. siderite is also present in ST21 G09).

An alternative explanation is that these carbonates may not have precipitated in equilibrium with the ambient environment, and other factors (e.g. precipitation kinetics, different water composition) may have influenced the oxygen isotope fractionation (Leng and Marshall, 2004). The present dataset is too small to fully evaluate any systematic variations in isotopic characteristics within and between the samples. However, the data do suggest that there may be some potentially significant differences between the different types of carbonate cements observed in these MDAC samples, and it is recommended that a more detailed investigation should be undertaken to further characterise these MDAC sediments.

Table 6. Stable isotope analyses ($\delta^{13}\text{C}$ and $\delta^{18}\text{O}$) for bulk and microsampled carbonate components from the MDAC samples

Sample/Subsample No.	$\delta^{13}\text{C}_{\text{PDB}}$ (‰)	$\delta^{18}\text{O}_{\text{PDB}}$ (‰)	Mineral	Description
ST12 SLEDGE/1	-2.48	+3.25	CALCITE	Bioclast - bivalve shell
ST12 SLEDGE/2	-44.47	+2.55	ARAGONITE	Porous area with fibrous aragonite fringe cement
ST12 SLEDGE/3	-44.57	+2.61	ARAGONITE	Porous area with fibrous aragonite fringe cement
ST12 SLEDGE/4	-44.86	+2.52	ARAGONITE	Densely-cemented area with low porosity
ST12 SLEDGE/5	-46.94	+2.51	ARAGONITE	Bulk sample
ST21 GO9/1	FAIL	FAIL	DOLOMITE	Outer edge of sample - very fine laminated outer coating
ST21 GO9/2	-39.40	+1.77	DOLOMITE	Outer edge of sample - dense matrix cement dolomite with later siderite overgrowth
ST21 GO9/3	-46.95	+3.54	DOLOMITE	Centre of sample - porous band with grain-coating cement - dolomite only
ST21 GO9/4	-50.19	+3.91	DOLOMITE	Bulk sample
ST22 GO5/1	FAIL	FAIL	DOLOMITE	Centre of sample patchy spherulitic cement
ST22 GO5/2	FAIL	FAIL	DOLOMITE	Very porous area edge of sample - grain fringe cement
ST22 GO5/3	-50.34	+3.44	DOLOMITE	Densely cemented area - dominantly pore-filling cement
ST22 GO5/4	-48.79	+2.31	DOLOMITE	Porous area - dominantly grain coating fringe cement
ST22 GO5/5	-50.37	+3.13	DOLOMITE	Bulk sample
ST27 G22 1	FAIL	FAIL	ARAGONITE + HIGH MAG CALCITE	Very porous area - sparse aragonite coatings on Mg-calcite pellets
ST27 G22 2	-43.25	+3.74	HIGH MAG CALCITE	Densely cemented area - Mg-calcite only
ST27 G22 3	FAIL	FAIL	ARAGONITE	Edge of densely cemented area - sparse fibrous aragonite coatings
ST27 G22 4	-46.81	+2.72	ARAGONITE + HIGH MAG CALCITE	Edge of densely cemented area - Mg-calcite with aragonite fringes
ST27 G22 5	FAIL	FAIL	ARAGONITE	Edge of densely cemented area - sparse fibrous aragonite coatings
ST27 G22 6	-44.83	+2.97	HIGH MAG CALCITE	Bulk sample
ST35 G17 1	+2.38	+2.63	CALCITE	Bioclast - bivalve shell
ST35 G17 2	FAIL	FAIL	CALCITE	Bioclast - bivalve shell
ST35 G17 3	FAIL	FAIL	HIGH MAG CALCITE	Densely cemented area - matrix cement - edge of sample
ST35 G17 4	FAIL	FAIL	HIGH MAG CALCITE	Weakly-cemented porous area - grain-coating cement - middle of sample
ST35 G17 5	FAIL	FAIL	HIGH MAG CALCITE	Patchily-cemented area - matrix cement - middle of sample
ST35 G17 6	-44.29	+4.34	HIGH MAG CALCITE	Bulk sample

Sample/Subsample No.	$\delta^{13}\text{C}_{\text{PDB}}$ (‰)	$\delta^{18}\text{O}_{\text{PDB}}$ (‰)	Mineral	Description
ST36 RDO4 1	-32.31	+2.33	HIGH MAG CALCITE	Densely cemented area - close to edge of sample
ST36 RDO4 2	-36.64	+2.54	HIGH MAG CALCITE	Centre of sample - porous area with pelleted carbonate
ST36 RDO4 3	-34.20	+2.45	HIGH MAG CALCITE	Densely cemented area - close to edge of sample
ST36 RDO4 4	-31.19	+2.08	HIGH MAG CALCITE	Bulk sample

Note: "FAIL" denotes too little carbonate phase was present within the microdrill sample for detection and analysis

Summary and conclusions

Six samples of carbonate-cemented sandy sediment, recovered from the seabed of the Mid Irish Sea during a survey of the Mid Irish Sea area (Cefas Cruise CEND 11/08), have been characterised mineralogically and isotopically to describe the nature and evaluate the origin of the carbonate cement. The study forms part of an assessment of the geomorphology, and the distribution and range of seabed habitats, within this area of interest. The survey is focussed on identifying and delineating habitats listed under Annex I of the 1992 EC Habitats Directive; in particular, the Annex I habitat *Submarine structures made by leaking gases* (Whormersley *et al.*, 2008).

The carbonate-cemented sediments can be categorised into three principal end-member types:

1. *Aragonite-dominated cements*. This is exemplified by sample ST12 Sledge, which is a sandy sediment cemented by a sequence of aragonite cements comprising:
 - a Early isopachous grain-coating aragonite fringes coating detrital grains
 - b Precipitation of “clots”, or framboidal microbotryoidal aggregates of micritic or microcrystalline aragonite. These may coalesce to form a locally dense micritic matrix.
 - c Late-stage precipitation of acicular aragonite lining open pores and cavities in the cemented sandstone.
 - d The aragonite is strontium-rich with up to 2 mole% SrCO₃ in solid-solution
2. *High-magnesium calcite-dominated cements*. This is exemplified by sample ST35 G17, which displays:
 - a Early isopachous grain-coating high-magnesium calcite fringes coating detrital grains
 - b Precipitation of “clots”, or framboidal microbotryoidal aggregates of micritic or microcrystalline high-magnesium calcite, similar to the fabrics observed in the aragonite-dominant cemented sample ST12 Sledge. These micrite aggregates may coalesce to form a locally dense micritic matrix.
3. *Dolomite-dominated cements*. This is exemplified by samples ST21 G09 and ST22 G05. The carbonate fabrics are very similar to those encountered in the aragonite-dominated and high-magnesium calcite-dominated samples, with:
 - a Early isopachous grain-coating dolomite fringes
 - b Precipitation of “clots”, or framboidal microbotryoidal aggregates of micritic or microcrystalline dolomite, which may coalesce to form a locally dense micritic matrix.

The dolomite is a high-calcium dolomite which contains up to 10 mole% excess CaCO₃ relative to ideal stoichiometric dolomite. This may indicate that the dolomite is relatively poorly ordered and/or metastable, and may have precipitated rapidly (Vahrenkamp and Swart, 1994) possibly forming via a “protodolomite” precursor (*cf.* Deer *et al.*, 1992). Minor late-stage magnesium siderite was also found filling porosity in the dolomite cement and as overgrowths on dolomite crystals in sample ST21 G09. However, siderite was not found in any other samples.

Sample ST27 G22 can be regarded as a “hybrid” of Type 1 Type 2 carbonates. It consists of sandy sediment with high-magnesium calcite cements similar to those found in type 2.

However, it displays the development of later-stage acicular aragonite cement lining open intergranular pores, similar to the late-stage aragonite found in Type 1 carbonates.

Sample ST36 RD04 has a distinctly different type of carbonate fabric. It contains abundant sand-grade pelloidal grains consisting of intimately admixed micritic high-magnesium calcite and abundant siliciclastic silt and clay. It is interpreted to represent carbonate-rich sediment that has biologically-reworked and incorporated into faecal pellets. Apart from minor development of fine grain-coating high-magnesium calcite, petrographical evidence suggests that most of the carbonate cement in this sample has not precipitated in situ.

Stable isotope analyses of the carbonate cements shows that they are strong depleted in ^{13}C , ($\delta^{13}\text{C}_{\text{PDB}}$ values are range from -31 to -51%), which is consistent with a diagenetic origin in which carbonate precipitation is related to methane oxidation. This is very characteristic of MDAC reported from elsewhere (Jensen *et al.*, 1992; Sakai *et al.*, 1992; Bohrmann *et al.*, 1998; Peckmann *et al.*, 2001; Muralidhar *et al.*, 2006; Forsberg *et al.*, 2007), and supports the conclusion that these Mid Irish Sea seabed carbonates also have an MDAC origin.

The $\delta^{18}\text{O}$ signature of the carbonate cements does not correspond to the composition of carbonates expected to precipitate under present-day seabed conditions. The aragonite and high-magnesium calcites –dominated MDAC samples are isotopically slightly heavier than in cements expected to have formed in equilibrium with present-day conditions. This may indicate that they formed under slightly cooler conditions than at present. The dolomite cements show a relatively wide range in $\delta^{18}\text{O}$ values varying from values close to that predicted to form in equilibrium with seawater under present-day temperatures to dolomite which is slightly lighter than expected. This may indicate formation under slightly warmer conditions than at present. Alternatively, the dolomite may have formed metastably and not in equilibrium with seawater, which possibly supported by the observation that the dolomite has significant excess calcium (possibly indicating metastable formation of dolomite via a protodolomite precursor).

Both $\delta^{18}\text{O}$ and $\delta^{13}\text{C}$ values for the carbonate sample ST36 RD04 are slightly heavier than for the other MDAC samples. This may indicate mixture with a component of carbonate precipitated with bicarbonate derived from more open marine water, which may be consistent with evidence that much of the carbonate in this sample has been reworked.

References

- BOHRMANN, G., GREINERT, J., SUESS, E. AND TORRES, M. 1998. Authigenic carbonates from the Cascadia subduction zone and their relation to gas hydrate stability. *Geology*, **26**, 647-650.
- CLAYPOOL, G.E. AND KAPLAN, I.R. 1974. The origin and distribution of methane in marine sediments. *In*: KAPLAN, I.R. (editor) *Natural Gases in Marine Sediments*, Plenum Press, New York, 99-140
- COLEMAN, M.L. 1985. Geochemistry of diagenetic non-silicate minerals: kinetic considerations. *In*: EGLINTON, G., CURTIS, C.D. MCKENZIE, D.P. AND MURCHISON, D.G. (editors). *Geochemistry of Buried Sediments*. The Royal Society, London, 39-54
- CROKER, P.F., KOZACHENKO, M. AND WHEELER, A.J. 2005. Gas-related seabed structures in the Western Irish Sea (IRL-SEA6). *Technical Report of the Petroleum Affairs Division of Ireland, produced for Strategic Environmental Assessment – SEA6*
- DEER, W.A., HOWIE, R.A. AND ZUSSMAN, J. 1962. *Rock Forming Minerals. Volume 5: Non-Silicates*. Longmans, London.
- DEER, W.A., HOWIE, R.A. AND ZUSSMAN, J. 1992. *An Introduction to the Rock Forming Minerals (2nd edition)*. Pearson Education Limited, Harlow, London.
- FORSBERG, C.F., PLANKE, S., TJELTA, T.I., SVANO, G., STROUT, J.M. AND SVENSEN, H. 2007. Formation of pockmarks in the Norwegian Channel. *Proceedings of the 6th International Offshore Site Investigation and Geotechnics Conference: Confronting New Challenges and Sharing Knowledge, 11-12 September 2007, London, UK*, 221-230.
- GOLDSTEIN, J.I., NEWBURY, D.E., ECHLIN, P., JOY, D.C., FIORI, C. AND LIFSHIN, E. 1981. *Scanning Electron Microscopy and X-Ray Microanalysis*. Plenum Press, New York.
- HAYS, P.D. AND GROSSMAN, E.L. 1991. Oxygen isotopes in meteoric calcite cements as indicators of continental paleoclimate. *Geology*, **19**, 441-444.
- HOVLAND, M. AND TALBOT, M.R. 1987. Hydrocarbon seeps in northern marine waters; their occurrence and effects. *Journal of Sedimentary Research*, **57**,
- JENSEN, P., AAGAARD, I., BURKE JR., R.A., DANDO, P.R., JØGENSEN, N.O., KUIJPERS, A., LAIER, T., O'HARA, S.C.M. AND SCHMALJOHANN, R. 1992. 'Bubbling reefs' in the Kattegat: submarine landscapes of carbonate-cemented rocks support a diverse ecosystem at methane seeps. *Marine Ecology Progress Series*, **83**, 103-112.
- JNCC. 2003. *Irish Sea Pilot*. Joint Nature Conservation Committee (JNCC). [http://www.jncc.gov.uk/pdf/irish_finalreport\(maps\).pdf](http://www.jncc.gov.uk/pdf/irish_finalreport(maps).pdf)
- JUDD, A.G. 2005. The distribution and extent of methane-derived authigenic carbonate. *DTI Strategic Environmental Assessment, Area 6 (SEA6)*. United Kingdom Department of Trade and Industry (Dti)
- KIM, S.T. AND O'NEIL, J.R., 1997. Equilibrium and non-equilibrium oxygen isotope effects in synthetic carbonates. *Geochimica et Cosmochimica Acta*, **61**, 3461–3475.

- LAND, L.S., 1980. The isotopic and trace element geochemistry of dolomite: the state of the art. In: ZENGER, D.H., ET AL. (Editor.), *Concepts and Models of Dolomitisation*, Society of Economic Paleontologists and Mineralogists (SEPM), *Special Publication*, **28**, 87–110, Tulsa, Oklahoma.
- LENG, M.J. AND MARSHALL, J.D. 2004. Palaeoclimate interpretation of stable isotope data from lake sediment archives. *Quaternary Science Reviews*, **23**, 811-831.
- MARSHALL, J.D. 1988. *Cathodoluminescence of Geological Materials*. Allen & Unwin Inc., USA.
- MILODOWSKI, A.E. TULLBORG, E.-L., BUIL, B., GÓMEZ, P., TURRERO, M.-J., HASZELDINE, S., ENGLAND, G., GILLESPIE, M.R., TORRES, T., ORTIZ, J.E., ZACHARIÁŠ, SILAR, J., CHVÁTAL, M., STRNAD, L., ŠEBEK, O. BOUCH, J.E., CHENERY, S.R., CHENERY, C., SHEPHERD, T.J. AND MCKERVEY, J.A. 2005. Application of Mineralogical, Petrological and Geochemical tools for Evaluating the Palaeohydrogeological Evolution of the PADAMOT Study Sites. PADAMOT PROJECT - EU FP5 CONTRACT NO. FIKW-CT2001-20129. *PADAMOT Project Technical Report, WP2*. 228pp +digital appendices.
- MOZLEY, P.S. 1989. Relation between depositional environment and the elemental composition of early diagenetic siderite. *Geology*, **17**, 704-706.
- MOZLEY, P. AND BURNS, S.J. 1993. Oxygen and carbon isotope comparison of marine carbonate concretions: an overview. *Journal of Sedimentary Petrology*, **63**, 73-83.
- MURALIDHAR, K., MAZUMDAR, A., KARISIDDAIAH, S.M., BOROLE, D.V. AND RAO, B.R. 2006. evidences of methane-derived authigenic carbonates from the sediments of the Krishna-Godavari Basin, eastern continental margin of India. *Current Science*, **91**, 318-323.
- O'NEIL, J.R., CLAYTON, R.N. AND MAYEDA, T.K. 1969. Oxygen isotope fractionation in divalent metal carbonates. *Journal of Chemical Physics*, **51**, 5547-5558.
- PECKMANN, J., REIMER, A., LUTH, U., HANSEN, B.T., HEINICKE, C., HOEFS, J. AND REITNER, J. 2001. Methane-derived carbonates and authigenic pyrite from the northwestern Black Sea. *Marine Geology*, **177**, 129-150.
- PIRRIE, D AND MARSHALL, J.D. 1991. Field relationships and stable isotope geochemistry of concretions from James Ross Island, Antarctica. *Sedimentary Geology*, **71**, 137-150.
- SAKAI, H., GAMO, T., OGAWA, Y. AND BOULEGUE, J. 1992. Stable isotope ratios and origins of the carbonates associated with cold seepage at the eastern Nankai Trough: fluids in convergent margins. *Earth and Planetary Science Letters*, **3-4**, 391-404.
- TARUTANI, T., CLAYTON, R.N., AND MAYEDA, T. 1969. The effect of polymorphism and magnesium substitution on oxygen isotope fractionation between calcium carbonate and water. *Geochimica et Cosmochimica Acta*, **33**, 987–996.

VAHRENKAMP, V.C. AND SWART, P.K. 1994. Late Cenozoic dolomites of the Bahamas: metastable analogues for the genesis of ancient platform dolomites. *Special Publication of the International Association of Sedimentologists*, **21**, 133-153.

WHORMERSLEY, P., WILSON, C., LIMPENNY, D. AND LESLIE, A. 2008. Understanding the marine environment – seabed habitat investigations of Submarine structures in the mid-Irish Sea and Solan Bank Area of Search (AoS) – cruise report. JNCC Contract No: F90-01-1200. *CEFAS Cruise Report CEND 11/08*, 120pp. JNCC CONTRACT NO: F90-01-1200